PHYSICAL REVIEW D **84,** 052006 (2011)

Measurement of the cross section for prompt isolated diphoton production in $p\bar{p}$ collisions at $\sqrt{s} = 1.96$ TeV

T. Aaltonen,[21] B. Álvarez González,[9,w] S. Amerio,[41a] D. Amidei,[32] A. Anastassov,[36] A. Annovi,[17] J. Antos,[12] G. Apollinari,[15] J. A. Appel,[15] A. Apresyan,[46] T. Arisawa,[56] A. Artikov,[13] J. Asaadi,[51] W. Ashmanskas,[15] B. Auerbach,[59] A. Aurisano,[51] F. Azfar,[40] W. Badgett,[15] A. Barbaro-Galtieri,[26] V. E. Barnes,[46] B. A. Barnett,[23] P. Barria,[44c,44a] P. Bartos,[12] M. Bauce,[41b,41a] G. Bauer,[30] F. Bedeschi,[44a] D. Beecher,[28] S. Behari,[23] G. Bellettini,[44b,44a] J. Bellinger,[58] D. Benjamin,[14] A. Beretvas,[15] A. Bhatti,[48] M. Binkley,[15,a] D. Bisello,[41b,41a] I. Bizjak,[28,aa] K. R. Bland,[a5] B. Blumenfeld,[23] A. Bocci,[14] A. Bodek,[47] D. Bortoletto,[46] J. Boudreau,[45] A. Boveia,[11] B. Brau,[15,b] L. Brigliadori,[a6b,6a] A. Brisuda,[12] C. Bromberg,[33] E. Brucken,[21] M. Bucciantonio,[44b,44a] J. Budagov,[13] H. S. Budd,[47] S. Budd,[22] K. Burkett,[15] G. Busetto,[41b,41a] P. Bussey,[19] A. Buzatu,[31] C. Calancha,[29] S. Camarda,[a4] M. Campanelli,[33] M. Campbell,[32] F. Canelli,[12,15] A. Canepa,[43] B. Carls,[22] D. Carlsmith,[58] R. Carosi,[44a] S. Carrillo,[16,l] S. Carron,[15] B. Casal,[9] M. Casarsa,[15] A. Castro,[a6b,6a] P. Catastini,[15] D. Cauz,[52a] V. Cavaliere,[44c,44a] M. Cavalli-Sforza,[a4] A. Cerri,[26,g] L. Cerrito,[28,r] Y. C. Chen,[a1] M. Chertok,[7] G. Chiarelli,[44a] G. Chlachidze,[15] F. Chlebana,[15] K. Cho,[25] D. Chokheli,[13] J. P. Chou,[20] W. H. Chung,[58] Y. S. Chung,[47] C. I. Ciobanu,[42] M. A. Ciocci,[44c,44a] A. Clark,[18] G. Compostella,[41b,41a] M. E. Convery,[15] J. Conway,[7] M. Corbo,[42] M. Cordelli,[17] C. A. Cox,[7] D. J. Cox,[7] F. Crescioli,[44b,44a] C. Cuenca Almenar,[59] J. Cuevas,[9,w] R. Culbertson,[15] D. Dagenhart,[15] N. d'Ascenzo,[42,u] M. Datta,[15] P. de Barbaro,[47] S. De Cecco,[49a] G. De Lorenzo,[a4] M. Dell'Orso,[44b,44a] C. Deluca,[a4] L. Demortier,[48] J. Deng,[14,d] M. Deninno,[6a] F. Devoto,[21] M. d'Errico,[41b,41a] A. Di Canto,[44b,44a] B. Di Ruzza,[44a] J. R. Dittmann,[a5] M. D'Onofrio,[27] S. Donati,[44b,44a] P. Dong,[15] M. Dorigo,[52a] T. Dorigo,[41a] K. Ebina,[56] A. Elagin,[51] A. Eppig,[32] R. Erbacher,[7] D. Errede,[22] S. Errede,[22] N. Ershaidat,[42,z] R. Eusebi,[51] H. C. Fang,[26] S. Farrington,[40] M. Feindt,[24] J. P. Fernandez,[29] C. Ferrazza,[44d,44a] R. Field,[16] G. Flanagan,[46,s] R. Forrest,[7] M. J. Frank,[a5] M. Franklin,[20] J. C. Freeman,[15] Y. Funakoshi,[56] I. Furic,[16] M. Gallinaro,[48] J. Galyardt,[10] J. E. Garcia,[18] A. F. Garfinkel,[46] P. Garosi,[44c,44a] H. Gerberich,[22] E. Gerchtein,[15] S. Giagu,[49b,49a] V. Giakoumopoulou,[a3] P. Giannetti,[44a] K. Gibson,[45] C. M. Ginsburg,[15] N. Giokaris,[a3] P. Giromini,[17] M. Giunta,[44a] G. Giurgiu,[23] V. Glagolev,[13] D. Glenzinski,[15] M. Gold,[35] D. Goldin,[51] N. Goldschmidt,[16] A. Golossanov,[15] G. Gomez,[9] G. Gomez-Ceballos,[30] M. Goncharov,[30] O. González,[29] I. Gorelov,[35] A. T. Goshaw,[14] K. Goulianos,[48] A. Gresele,[41a] S. Grinstein,[a4] C. Grosso-Pilcher,[11] R. C. Group,[55] J. Guimaraes da Costa,[20] Z. Gunay-Unalan,[33] C. Haber,[26] S. R. Hahn,[15] E. Halkiadakis,[50] A. Hamaguchi,[39] J. Y. Han,[47] F. Happacher,[17] K. Hara,[53] D. Hare,[50] M. Hare,[54] R. F. Harr,[57] K. Hatakeyama,[a5] C. Hays,[40] M. Heck,[24] J. Heinrich,[43] M. Herndon,[58] S. Hewamanage,[a5] D. Hidas,[50] A. Hocker,[15] W. Hopkins,[15,h] D. Horn,[24] S. Hou,[a1] R. E. Hughes,[37] M. Hurwitz,[11] U. Husemann,[59] N. Hussain,[31] M. Hussein,[33] J. Huston,[33] G. Introzzi,[44a] M. Iori,[49b,49a] A. Ivanov,[7,p] E. James,[15] D. Jang,[10] B. Jayatilaka,[14] E. J. Jeon,[25] M. K. Jha,[6a] S. Jindariani,[15] W. Johnson,[7] M. Jones,[46] K. K. Joo,[25] S. Y. Jun,[10] T. R. Junk,[15] T. Kamon,[51] P. E. Karchin,[57] Y. Kato,[39,o] W. Ketchum,[11] J. Keung,[43] V. Khotilovich,[51] B. Kilminster,[15] D. H. Kim,[25] H. S. Kim,[25] H. W. Kim,[25] J. E. Kim,[25] M. J. Kim,[17] S. B. Kim,[25] S. H. Kim,[53] Y. K. Kim,[11] N. Kimura,[56] M. Kirby,[15] S. Klimenko,[16] K. Kondo,[56] D. J. Kong,[25] J. Konigsberg,[16] A. V. Kotwal,[14] M. Kreps,[24] J. Kroll,[43] D. Krop,[11] N. Krumnack,[a5,m] M. Kruse,[14] V. Krutelyov,[51,e] T. Kuhr,[24] M. Kurata,[53] S. Kwang,[11] A. T. Laasanen,[46] S. Lami,[44a] S. Lammel,[15] M. Lancaster,[28] R. L. Lander,[7] K. Lannon,[37,v] A. Lath,[50] G. Latino,[44a,d] I. Lazzizzera,[41a] T. LeCompte,[a2] E. Lee,[51] H. S. Lee,[11] J. S. Lee,[25] S. W. Lee,[51,x] S. Leo,[44b,44a] S. Leone,[44a] J. D. Lewis,[15] C.-J. Lin,[26] J. Linacre,[40] M. Lindgren,[15] E. Lipeles,[43] A. Lister,[18] D. O. Litvintsev,[15] C. Liu,[45] Q. Liu,[46] T. Liu,[15] S. Lockwitz,[59] N. S. Lockyer,[43] A. Loginov,[59] D. Lucchesi,[41b,41a] J. Lueck,[24] P. Lujan,[26] P. Lukens,[15] G. Lungu,[48] J. Lys,[26] R. Lysak,[12] R. Madrak,[15] K. Maeshima,[15] K. Makhoul,[30] P. Maksimovic,[23] S. Malik,[48] G. Manca,[27,c] A. Manousakis-Katsikakis,[a3] F. Margaroli,[46] C. Marino,[24] M. Martínez,[a4] R. Martínez-Ballarín,[29] P. Mastrandrea,[49a] M. Mathis,[23] M. E. Mattson,[57] P. Mazzanti,[6a] K. S. McFarland,[47] P. McIntyre,[51] R. McNulty,[27,j] A. Mehta,[27] P. Mehtala,[21] A. Menzione,[44a] C. Mesropian,[48] T. Miao,[15] D. Mietlicki,[32] A. Mitra,[a1] H. Miyake,[53] S. Moed,[20] N. Moggi,[6a] M. N. Mondragon,[15,l] C. S. Moon,[25] R. Moore,[15] M. J. Morello,[15] J. Morlock,[24] P. Movilla Fernandez,[15] A. Mukherjee,[15] Th. Muller,[24] P. Murat,[15] M. Mussini,[a6b,6a] J. Nachtman,[15,n] Y. Nagai,[53] J. Naganoma,[56] I. Nakano,[38] A. Napier,[54] J. Nett,[51] C. Neu,[55] M. S. Neubauer,[22] J. Nielsen,[26,f] L. Nodulman,[a2] O. Norniella,[22] E. Nurse,[28] L. Oakes,[40] S. H. Oh,[14] Y. D. Oh,[25] I. Oksuzian,[55] T. Okusawa,[39] R. Orava,[21] L. Ortolan,[a4] S. Pagan Griso,[41b,41a] C. Pagliarone,[52a] E. Palencia,[9,g] V. Papadimitriou,[15] A. A. Paramonov,[a2] J. Patrick,[15] G. Pauletta,[52a,g] M. Paulini,[10] C. Paus,[30] D. E. Pellett,[7] A. Penzo,[52a] T. J. Phillips,[14] G. Piacentino,[44a] E. Pianori,[43] J. Pilot,[37] K. Pitts,[22] C. Plager,[8] L. Pondrom,[58] K. Potamianos,[46] O. Poukhov,[13,a] A. Pranko,[60] F. Prokoshin,[13,y] F. Ptohos,[17,i] E. Pueschel,[10] G. Punzi,[44b,44a] J. Pursley,[58] A. Rahaman,[45] V. Ramakrishnan,[58] N. Ranjan,[46] I. Redondo,[29] P. Renton,[40] M. Rescigno,[49a] F. Rimondi,[a6b,6a] L. Ristori,[44a,15]

1550-7998/2011/84(5)/052006(32)

A. Robson,[19] T. Rodrigo,[9] T. Rodriguez,[43] E. Rogers,[22] S. Rolli,[54] R. Roser,[15] M. Rossi,[52a] F. Rubbo,[15] F. Ruffini,[44c,44a] A. Ruiz,[9] J. Russ,[10] V. Rusu,[15] A. Safonov,[51] W. K. Sakumoto,[47] Y. Sakurai,[56] L. Santi,[52b,52a] L. Sartori,[44a] K. Sato,[53] V. Saveliev,[42,u] A. Savoy-Navarro,[42] P. Schlabach,[15] A. Schmidt,[24] E. E. Schmidt,[15] M. P. Schmidt,[59,a] M. Schmitt,[36] T. Schwarz,[7] L. Scodellaro,[9] A. Scribano,[44c,44a] F. Scuri,[44a] A. Sedov,[46] S. Seidel,[35] Y. Seiya,[39] A. Semenov,[13] F. Sforza,[44b,44a] A. Sfyrla,[22] D. Sgalaberna,[a6b] S. Z. Shalhout,[7] T. Shears,[27] P. F. Shepard,[45] M. Shimojima,[53,t] S. Shiraishi,[11] M. Shochet,[11] I. Shreyber,[34] A. Simonenko,[13] P. Sinervo,[31] A. Sissakian,[13,a] K. Sliwa,[54] J. R. Smith,[7] F. D. Snider,[15] A. Soha,[15] S. Somalwar,[50] V. Sorin,[a4] P. Squillacioti,[15] M. Stancari,[15] M. Stanitzki,[59] R. St. Denis,[19] B. Stelzer,[31] O. Stelzer-Chilton,[31] D. Stentz,[36] J. Strologas,[35] G. L. Strycker,[32] Y. Sudo,[53] A. Sukhanov,[16] I. Suslov,[13] K. Takemasa,[53] Y. Takeuchi,[53] J. Tang,[11] M. Tecchio,[32] P. K. Teng,[a1] J. Thom,[15,h] J. Thome,[10] G. A. Thompson,[22] E. Thomson,[43] P. Ttito-Guzmán,[29] S. Tkaczyk,[15] D. Toback,[51] S. Tokar,[12] K. Tollefson,[33] T. Tomura,[53] D. Tonelli,[15] S. Torre,[17] D. Torretta,[15] P. Totaro,[52b,52a] M. Trovato,[44d,44a] Y. Tu,[43] F. Ukegawa,[53] S. Uozumi,[25] A. Varganov,[32] F. Vázquez,[16,l] G. Velev,[15] C. Vellidis,[a3] M. Vidal,[29] I. Vila,[9] R. Vilar,[9] J. Vizán,[9] M. Vogel,[35] G. Volpi,[44b,44a] P. Wagner,[43] R. L. Wagner,[15] T. Wakisaka,[39] R. Wallny,[8] S. M. Wang,[a1] A. Warburton,[31] D. Waters,[28] M. Weinberger,[51] W. C. Wester III,[15] B. Whitehouse,[54] D. Whiteson,[43,d] A. B. Wicklund,[a2] E. Wicklund,[15] S. Wilbur,[11] F. Wick,[24] H. H. Williams,[43] J. S. Wilson,[37] P. Wilson,[15] B. L. Winer,[37] P. Wittich,[15,h] S. Wolbers,[15] H. Wolfe,[37] T. Wright,[32] X. Wu,[18] Z. Wu,[a5] K. Yamamoto,[39] J. Yamaoka,[14] T. Yang,[15] U. K. Yang,[11,q] Y. C. Yang,[25] W.-M. Yao,[26] G. P. Yeh,[15] K. Yi,[15,n] J. Yoh,[15] K. Yorita,[56] T. Yoshida,[39,k] G. B. Yu,[14] I. Yu,[25] S. S. Yu,[15] J. C. Yun,[15] A. Zanetti,[52a] Y. Zeng,[14] and S. Zucchelli[a6b,6a]

(CDF Collaboration)

[a1]*Institute of Physics, Academia Sinica, Taipei, Taiwan 11529, Republic of China*
[a2]*Argonne National Laboratory, Argonne, Illinois 60439, USA*
[a3]*University of Athens, 157 71 Athens, Greece*
[a4]*Institut de Fisica d'Altes Energies, ICREA, Universitat Autonoma de Barcelona, E-08193, Bellaterra (Barcelona), Spain*
[a5]*Baylor University, Waco, Texas 76798, USA*
[6a]*Istituto Nazionale di Fisica Nucleare Bologna, I-40127 Bologna, Italy*
[a6b]*University of Bologna, I-40127 Bologna, Italy*
[7]*University of California, Davis, Davis, California 95616, USA*
[8]*University of California, Los Angeles, Los Angeles, California 90024, USA*
[9]*Instituto de Fisica de Cantabria, CSIC-University of Cantabria, 39005 Santander, Spain*
[10]*Carnegie Mellon University, Pittsburgh, Pennsylvania 15213, USA*
[11]*Enrico Fermi Institute, University of Chicago, Chicago, Illinois 60637, USA*
[12]*Comenius University, 842 48 Bratislava, Slovakia; Institute of Experimental Physics, 040 01 Kosice, Slovakia*
[13]*Joint Institute for Nuclear Research, RU-141980 Dubna, Russia*
[14]*Duke University, Durham, North Carolina 27708, USA*
[15]*Fermi National Accelerator Laboratory, Batavia, Illinois 60510, USA*
[16]*University of Florida, Gainesville, Florida 32611, USA*
[17]*Laboratori Nazionali di Frascati, Istituto Nazionale di Fisica Nucleare, I-00044 Frascati, Italy*
[18]*University of Geneva, CH-1211 Geneva 4, Switzerland*
[19]*Glasgow University, Glasgow G12 8QQ, United Kingdom*
[20]*Harvard University, Cambridge, Massachusetts 02138, USA*
[21]*Division of High Energy Physics, Department of Physics, University of Helsinki and Helsinki Institute of Physics, FIN-00014, Helsinki, Finland, USA*
[22]*University of Illinois, Urbana, Illinois 61801, USA*
[23]*The Johns Hopkins University, Baltimore, Maryland 21218, USA*
[24]*Institut für Experimentelle Kernphysik, Karlsruhe Institute of Technology, D-76131 Karlsruhe, Germany*
[25]*Center for High Energy Physics: Kyungpook National University, Daegu 702-701, Korea; Seoul National University, Seoul 151-742, Korea; Sungkyunkwan University, Suwon 440-746, Korea; Korea Institute of Science and Technology Information, Daejeon 305-806, Korea; Chonnam National University, Gwangju 500-757, Korea; Chonbuk National University, Jeonju 561-756, Korea*
[26]*Ernest Orlando Lawrence Berkeley National Laboratory, Berkeley, California 94720, USA*
[27]*University of Liverpool, Liverpool L69 7ZE, United Kingdom*
[28]*University College London, London WC1E 6BT, United Kingdom*
[29]*Centro de Investigaciones Energeticas Medioambientales y Tecnologicas, E-28040 Madrid, Spain*
[30]*Massachusetts Institute of Technology, Cambridge, Massachusetts 02139, USA*

[31]*Institute of Particle Physics: McGill University, Montréal, Québec, Canada H3A 2T8; Simon Fraser University, Burnaby, British Columbia, Canada V5A 1S6; University of Toronto, Toronto, Ontario, Canada M5S 1A7; and TRIUMF, Vancouver, British Columbia, Canada V6T 2A3*
[32]*University of Michigan, Ann Arbor, Michigan 48109, USA*
[33]*Michigan State University, East Lansing, Michigan 48824, USA*
[34]*Institution for Theoretical and Experimental Physics, ITEP, Moscow 117259, Russia*
[35]*University of New Mexico, Albuquerque, New Mexico 87131, USA*
[36]*Northwestern University, Evanston, Illinois 60208, USA*
[37]*The Ohio State University, Columbus, Ohio 43210, USA*
[38]*Okayama University, Okayama 700-8530, Japan*
[39]*Osaka City University, Osaka 588, Japan*
[40]*University of Oxford, Oxford OX1 3RH, United Kingdom*
[41a]*Istituto Nazionale di Fisica Nucleare, Sezione di Padova-Trento, I-35131 Padova, Italy*
[41b]*University of Padova, I-35131 Padova, Italy*
[42]*LPNHE, , USAUniversite Pierre et Marie Curie/IN2P3-CNRS, UMR7585, Paris, F-75252 France*
[43]*University of Pennsylvania, Philadelphia, Pennsylvania 19104, USA*
[44a]*Istituto Nazionale di Fisica Nucleare Pisa, I-56127 Pisa, Italy*
[44b]*University of Pisa, I-56127 Pisa, Italy*
[44c]*University of Siena, I-56127 Pisa, Italy*
[44d]*Scuola Normale Superiore, I-56127 Pisa, Italy*
[45]*University of Pittsburgh, Pittsburgh, Pennsylvania 15260, USA*
[46]*Purdue University, West Lafayette, Indiana 47907, USA*
[47]*University of Rochester, Rochester, New York 14627, USA*
[48]*The Rockefeller University, New York, New York 10065, USA*
[49a]*Istituto Nazionale di Fisica Nucleare, Sezione di Roma 1, I-00185 Roma, Italy*
[49b]*Sapienza Università di Roma, I-00185 Roma, Italy*
[50]*Rutgers University, Piscataway, New Jersey 08855, USA*
[51]*Texas A&M University, College Station, Texas 77843, USA*
[52a]*Istituto Nazionale di Fisica Nucleare Trieste/Udine, I-34100 Trieste, Italy*
[52b]*University of Trieste/Udine, I-33100 Udine, Italy*
[53]*University of Tsukuba, Tsukuba, Ibaraki 305, Japan*
[54]*Tufts University, Medford, Massachusetts 02155, USA*
[55]*University of Virginia, Charlottesville, Virginia 22906, USA*
[56]*Waseda University, Tokyo 169, Japan*

---

[a]Deceased.
[b]With visitors from University of Massachusetts Amherst, Amherst, MA 01003, USA.
[c]With visitors from Istituto Nazionale di Fisica Nucleare, Sezione di Cagliari, 09042 Monserrato (Cagliari), Italy.
[d]With visitors from University of California Irvine, Irvine, CA 92697, USA.
[e]With visitors from University of California Santa Barbara, Santa Barbara, CA 93106, USA.
[f]With visitors from University of California Santa Cruz, Santa Cruz, CA 95064, USA.
[g]With visitors from CERN, CH- 1211 Geneva, Switzerland.
[h]With visitors from Cornell University, Ithaca, NY 14853, USA.
[i]With visitors from University of Cyprus, Nicosia CY-1678, Cyprus.
[j]With visitors from University College Dublin, Dublin 4, Ireland.
[k]With visitors from University of Fukui, Fukui City, Fukui Prefecture, Japan 910-0017.
[l]With visitors from Universidad Iberoamericana, Mexico D.F., Mexico.
[m]With visitors from Iowa State University, Ames, IA 50011, USA.
[n]With visitors from University of Iowa, Iowa City, IA 52242, USA.
[o]With visitors from Kinki University, Higashi-Osaka City, Japan 577-8502.
[p]With visitors from Kansas State University, Manhattan, KS 66506, USA.
[q]With visitors from University of Manchester, Manchester M13 9PL, England.
[r]With visitors from Queen Mary, University of London, London, E1 4NS, England.
[s]With visitors from Muons, Inc., Batavia, IL 60510, USA.
[t]With visitors from Nagasaki Institute of Applied Science, Nagasaki, Japan.
[u]With visitors from National Research Nuclear University, Moscow, Russia.
[v]With visitors from University of Notre Dame, Notre Dame, IN 46556, USA.
[w]With visitors from Universidad de Oviedo, E-33007 Oviedo, Spain.
[x]With visitors from Texas Tech University, Lubbock, TX 79609, USA.
[y]With visitors from Universidad Tecnica Federico Santa Maria, 110v Valparaiso, Chile.
[z]With visitors from Yarmouk University, Irbid 211-63, Jordan.
[aa]On leave from J. Stefan Institute, Ljubljana, Slovenia.

[57]*Wayne State University, Detroit, Michigan 48201, USA*
[58]*University of Wisconsin, Madison, Wisconsin 53706, USA*
[59]*Yale University, New Haven, Connecticut 06520, USA*
[60]*Ernest Orlando Lawrence Berkeley National Laboratory, Berkeley, California 9472 0, USA*
(Received 29 June 2011; published 15 September 2011)

This article reports a measurement of the production cross section of prompt isolated photon pairs in proton-antiproton collisions at $\sqrt{s} = 1.96$ TeV using the CDF II detector at the Fermilab Tevatron collider. The data correspond to an integrated luminosity of 5.36 fb^{-1}. The cross section is presented as a function of kinematic variables sensitive to the reaction mechanisms. The results are compared with three perturbative QCD calculations: (1) a leading-order parton shower Monte Carlo, (2) a fixed next-to-leading-order calculation and (3) a next-to-leading-order/next-to-next-to-leading-log resummed calculation. The comparisons show that, within their known limitations, all calculations predict the main features of the data, but no calculation adequately describes all aspects of the data.

DOI: 10.1103/PhysRevD.84.052006 PACS numbers: 13.85.Qk

I. INTRODUCTION

The measurement of the production cross section of two energetic isolated central photons (diphotons) in high energy hadron collisions is important for testing standard model predictions in the domain of searches for undiscovered particles and new physics. Understanding the reaction mechanisms in the complicated environment formed in such collisions is a challenge for perturbative quantum chromodynamics calculations. Photons originating from hard collisions of hadrons (''direct'' or ''prompt'' photons) are an ideal probe for testing these calculations because they do not interact with other final-state particles, and their energies and directions can be measured with high precision in modern electromagnetic calorimeters. Prompt diphoton production creates an irreducible background to the diphoton decay channel of proposed new particles, such as low mass Higgs bosons or Randall-Sundrum gravitons in models of extra spatial dimensions [1,2]. An improved knowledge of the standard model background will help the development of more powerful search strategies for these particles.

The basic mechanisms of prompt diphoton production in hadron collisions are quark-antiquark annihilation $q\bar{q} \to \gamma\gamma$, quark-gluon scattering $gq \to \gamma\gamma q$, and gluon-gluon fusion $gg \to \gamma\gamma$. The respective basic diagrams are shown in Fig. 1. At the Tevatron, the dominant mechanism is quark-antiquark annihilation. In quark-gluon scattering, most of the time at least one of the two photons is emitted almost parallel to the scattered quark. Contributions from this mechanism are therefore suppressed by requiring isolated prompt photons. Each mechanism can be modeled by calculating the respective matrix element for the specific event kinematics. Matrix element calculations of leading order (LO) in the strong coupling are relatively simple and are thus implemented in advanced parton shower Monte Carlo (MC) event generators [3–5], which allow for gluon and photon radiation as well as multiple interactions in the colliding beams. By including radiation before and after the hard scattering, parton shower generators take into account soft gluon and photon emissions, thus resulting in an effective resummation of all of the leading logarithmic terms in the cross section to all orders of the strong and electromagnetic couplings constants. Next-to-leading order (NLO) calculations [6–8] additionally include one-loop corrections at the cost of not featuring realistic multiparticle event representations as the LO generators do. Recent NLO calculations include an analytical resummation of the cross section for initial-state gluon radiation to all orders in the strong coupling constant [8], reaching a higher logarithmic accuracy than in the parton shower Monte Carlo generators. By this method, all soft gluon emissions in the initial state are taken into account, and reliable predictions for the low diphoton transverse momentum region are possible. A fixed-order NLO calculation implemented by the DIPHOX program [6] also accounts for the case where a final-state quark loses almost all of its energy to the photon detected in the event [9]. This process is called ''fragmentation'' and, in contrast to final-state photon radiation in parton showering, it involves nonperturbative calculations. One or both of the photons in the event may come from fragmentation. The case where both photons come from fragmentation of a single quark is also possible, but is not included in calculations, as in this case the photons are nearly collinear and nonisolated most of the time.

The prompt diphoton cross section has been previously measured by the CDF Collaboration using 200 pb^{-1} of data [10], but the large statistical uncertainties did not allow for a precise comparison with theoretical calculations. The nearly 30–times larger CDF II data set currently available presents an opportunity to significantly extend the kinematic range and perform a detailed study of diphoton kinematic distributions. A recent measurement of the diphoton cross section using 4.2 fb^{-1} has been reported by the D0 Collaboration [11]. The reported differential cross sections were only partly reproduced by theoretical calculations [3,6,8], although the discrepancies between the NLO calculations [6,8] and the data were less important

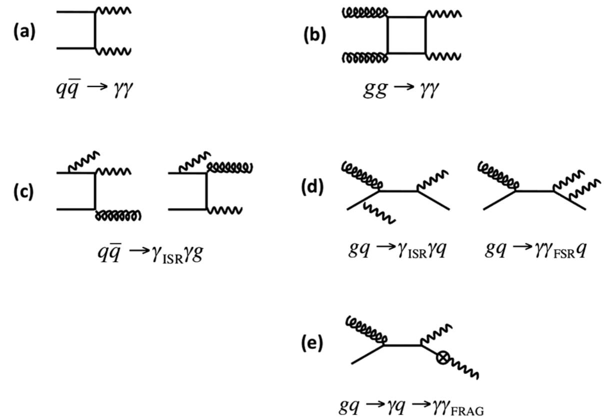

FIG. 1. Basic diagrams for prompt diphoton production: (a)-(b) direct, (c)-(d) one-photon radiation from an initial- (ISR) or final-state quark (FSR), (e) fragmentation where one photon is emitted along the direction of a final-state quark taking almost all of its energy. The symbol \otimes denotes the nonperturbative mechanism of the fragmentation process (FRAG).

in kinematic regions where the Higgs boson or new heavy particles are expected.

This article is organized as follows. An overview of the detector is given in Sec. II. The event selection is presented in Sec. III. Section IV deals with extracting the cross section from the selected diphoton sample. The results are presented and discussed in Sec. V. The conclusions are given in Sec. VI. Appendix A explains details of the nonprompt photon subtraction technique introduced in Sec. IV. Finally, tables of the measured cross section, differential in various kinematic quantities, are given in Appendix B.

II. DETECTOR OVERVIEW

The CDF II detector is a cylindrically-symmetric apparatus [12] designed to study $p\bar{p}$ collisions at the Fermilab Tevatron. The detector has been described in detail elsewhere [14]; only the detector components that are relevant to this analysis are briefly discussed here. The magnetic spectrometer consists of tracking devices inside a 3-m diameter, 5-m long superconducting solenoid magnet, which provides an axial magnetic field of 1.4 T. A set of silicon microstrip detectors (L00, SVX, and ISL) [15–17] and a 3.1-m long drift chamber (COT) [18] with 96 layers of sense wires measure momenta and trajectories (tracks) of charged particles in the pseudorapidity regions of $|\eta| < 2$ and $|\eta| < 1$ [12], respectively. Surrounding the magnet coil is the projective-tower-geometry sampling calorimeter, which is used to identify and measure the energy and direction of photons, electrons, and jets. The calorimeter consists of lead-scintillator electromagnetic and iron-scintillator hadron compartments and it is divided into a central barrel ($|\eta| < 1.1$) and a pair of "end plugs" that cover the region $1.1 < |\eta| < 3.6$. The central calorimeter is composed of towers with a segmentation of $\Delta\eta \times \Delta\phi \simeq 0.1 \times 15^o$. The energy resolution of the central electromagnetic calorimeter for electrons is $\sigma(E_{\rm T})/E_{\rm T} = 13.5\%/\sqrt{E_{\rm T}({\rm GeV})} \oplus 1.5\%$ [19], while the energy resolution of the central hadron calorimeter for charged pions that do not interact in the electromagnetic section is $\sigma(E_{\rm T})/E_{\rm T} = 50\%/\sqrt{E_{\rm T}({\rm GeV})} \oplus 3\%$ [20]. Multiwire proportional chambers with cathode-strip readout (the central electromagnetic shower maximum detector [CES] system), located at the depth of six radiation lengths (near shower maximum) in the central electromagnetic calorimeter, are used for identification and precise position measurement of photons and electrons. Cathode strips and anode wires, with a channel spacing between 1.5 cm and 2 cm, running along the azimuthal (strips) and the beam line (wires) direction provide location and two-dimensional profiles of electromagnetic showers. The position resolution of the CES is 2 mm for a 50 GeV photon. The electromagnetic compartments of the calorimeter are also used to measure the arrival time of particles depositing energy in each tower [21]. A system of Cherenkov luminosity counters [22], located around the beam pipe and inside the plug calorimeters, is used to measure the number of inelastic $p\bar{p}$ collisions per bunch crossing, and thereby the luminosity.

The online event selection at CDF is done by a three-level trigger [23] system with each level providing a rate reduction sufficient to allow for processing at the next level with minimal deadtime. Level 1 uses custom-designed hardware to find physics objects based on a subset of the detector information. Level 2 does limited event reconstruction. Level 3 uses the full detector information and consists of a farm of computers that reconstruct the data and apply selection criteria similar to the offline requirements.

III. DATA SELECTION AND EVENT RECONSTRUCTION

Inclusive $\gamma\gamma$ events are selected online by a three-level trigger that requires two isolated electromagnetic (EM) clusters with $E_{\rm T}^{\gamma} > 12$ GeV (diphoton-12 trigger) or two electromagnetic clusters with $E_{\rm T}^{\gamma} > 18$ GeV and no isolation requirement (diphoton-18 trigger). The transverse energy of the clusters is calculated with respect to the nominal center of the detector at $z = 0$ cm. The trigger requirements at each level are briefly described below.

At Level 1, events having two towers with EM $E_{\rm T} > 8$ GeV each are required. For each trigger tower, the amount of energy in the hadronic compartment of the calorimeter ($E^{\rm HAD}$) has to be consistent with that of an electromagnetic object. A trigger tower consists of two adjacent towers in the same calorimeter wedge, so that the granularity is approximately $\Delta\eta \times \Delta\phi \simeq 0.2 \times 15^o$.

The Level 2 requirements are different for the two triggers. The diphoton-12 trigger selects events if there are two isolated seeds with EM $E_T > 10$ GeV each. The isolation (ISO) energy is calculated as a sum of the transverse energy in the towers nearby the seed tower. The ISO energy for both photons has to be less than 3 GeV or 15% of the seed energy, whatever is larger. The diphoton-18 trigger requires two towers with EM $E_T > 16$ GeV each at Level 2.

Events are fully reconstructed at Level 3. At this level, for all photons in both triggers, the energy profile at the shower maximum of each photon candidate has to be consistent with that of a single photon. The diphoton-12 trigger selects events with two isolated photon candidates with $E_T > 12$ GeV. The isolation energy at Level 3 is calculated as the sum of E_T in all towers (except for photon towers) within the cone of $\Delta R = \sqrt{(\Delta\eta)^2 + (\Delta\phi)^2} < 0.4$ centered around the photon candidate. This ISO energy has to be less than 2 GeV or 10% of the photon energy, whatever is larger. The diphoton-18 trigger has no isolation requirement and accepts events with two photon candidates with $E_T > 18$ GeV. Table I gives a summary of all trigger requirements for events with EM objects in the central calorimeter and with E_T calculated with respect to the event vertex.

The triggered $\gamma\gamma$ candidate events are then subject to the offline selection. Each event is required to have two central photon candidates inside a well-instrumented region of the calorimeter (approximately $0.05 < |\eta| < 1.05$) with $E_T > 17$ GeV for one candidate and $E_T > 15$ GeV for the other. This asymmetric cut helps to avoid instabilities in fixed NLO calculations [6]. Photon candidates must satisfy strict (referred to as "tight") photon identification requirements. The EM cluster has to be located inside the well-instrumented region of the CES chamber, away from the ϕ-boundary of a calorimeter tower [24]. The energy deposition pattern in both transverse profiles at CES has to be consistent with that of a single electromagnetic object. The ratio of the energy measured in the hadron (HAD) calorimeter to the EM energy, E^{HAD}/E^{EM}, has to satisfy the requirement $E^{HAD}/E^{EM} < 0.055 + 0.00045 \times E^{\gamma}$. To distinguish photons from electrons, no high-p_T charged-particle track should point into the cluster ($N_{track} \leq 1$ with track $p_T < 1.0 + 0.005 \times E_T$). The main sources of "fake" photons are energetic π^0 and η^0 mesons produced in jets. These mesons are usually produced in association with other particles. To reduce this contamination from jets, the photon candidate must be isolated in the calorimeter. To calculate the calorimeter isolation (cal-ISO), the E_T deposited in the calorimeter towers within the cone of $\Delta R < 0.4$ around the EM cluster is summed, and the E_T of the EM cluster is subtracted. Cal-ISO is then corrected for the photon's energy leakage into towers in the neighboring wedge and for the contribution from multiple interactions in the same bunch crossing [25]. Cal-ISO must be consistent with the amount of energy expected from the underlying event (see Table II). In addition to the calorimeter isolation, there should be no other significant energy (E_T of 2nd CES cluster) deposited in the CES chamber containing the photon candidate. Table II provides a summary of the photon identification requirements described above. To reduce contamination due to cosmic-ray, beam-related, and other noncollision backgrounds, the event must contain a well-reconstructed vertex, formed from tracks, with $|z| < 60$ cm. If multiple vertices are reconstructed, the vertex with the largest $\sum p_T$ of the associated tracks is selected. The transverse energy of the photon candidates is calculated with respect to this primary vertex.

Inclusive $\gamma\gamma$ events satisfying the above criteria form the baseline $\gamma\gamma$ sample used in the analysis. Because of the presence of fakes, this sample consists of real $\gamma\gamma$, jet-γ, and *jet-jet* events. (An object misidentified as a photon is referred to as a fake photon.) Events with one or two fake photons are classified as background. The baseline signal plus background $\gamma\gamma$ sample consists of roughly 60 000 events in data corresponding to 5.36 fb^{-1} of integrated luminosity. Signal and background samples were simulated with the PYTHIA event generator, which includes simulation of the underlying event and multiple hadron interactions, as well as initial- (ISR) and final-state

TABLE I. Summary of the diphoton trigger requirements.

Trigger Level	Diphoton-12	Diphoton-18
	EM $E_T > 8$ GeV	same
Level 1	$E^{HAD}/E^{EM} < 0.125$	same
	$N_{cluster} = 2$	same
	EM $E_T > 10$ GeV	EM $E_T > 16$ GeV
Level 2	$E^{HAD}/E^{EM} < 0.125$	same
	$E_T^{ISO} < 3$ GeV or $E_T^{ISO}/E_T < 0.15$	not applied
	$N_{cluster} = 2$	same
	EM $E_T > 12$ GeV	EM $E_T > 18$ GeV
Level 3	$E^{HAD}/E^{EM} < 0.055 + 0.000\,45 \times E/\text{GeV}$ if $E < 200$ GeV	same
	$E_T^{ISO} < 2$ GeV or $E_T^{ISO}/E_T < 0.1$	not applied
	shower profile: $\chi^2_{CES} < 20$	same
	$N_{cluster} = 2$	same

TABLE II. Summary of the standard (tight) photon identification requirements for the $\gamma\gamma$ sample.

Cuts	Tight photon ID
Calorimeter fiduciality	central
E_T^γ	≥ 15 GeV ($1^{st}\gamma$), ≥ 17 GeV ($2^{nd}\gamma$)
Shower profile in CES: χ^2	≤ 20
E^{HAD}/E^{EM}	$\leq 0.055 + 0.00045 \times E/\text{GeV}$
cal-ISO	$\leq 0.1 \times E_T$ if $E_T < 20$ GeV or ≤ 2.0 GeV $+ 0.02 \times (E_T - 20$ GeV$)$
N_{tracks} in cluster	≤ 1
track p_T if $N_{tracks} = 1$	≤ 1.0 GeV $+ 0.005 \times E_T$
E_T of 2nd CES cluster	$\leq 0.14 \times E_T$ if $E_T < 18$ GeV ≤ 2.4 GeV $+ 0.01 \times E_T$ if $E_T \geq 18$ GeV

radiation (FSR) and a hadronization model of the final-state partons [3]. The PYTHIA events were processed through a GEANT-based detector simulation [26] and trigger emulation, followed by the same reconstruction program as that for the data.

IV. CROSS SECTION MEASUREMENT

This section describes the steps of the cross section measurement. Kinematic variables of interest are histogrammed to measure the corresponding differential cross section. The background is subtracted from each histogram bin. The signal histograms are normalized to the integrated luminosity and to the size of each bin to obtain uncorrected differential cross section histograms. These are then corrected for the reconstruction efficiency, acceptance, and resolution effects.

A. Background subtraction

The fake photon background subtraction is based on the use of the track isolation (track-ISO), which is calculated as the $\sum p_T$ of tracks with ΔR to the photon <0.4 and $|z_{vertex} - z_{track}| < 5$ cm. The concept of this technique is similar to the one used in the earlier measurement of the inclusive photon cross section [10]. The main idea behind the method is that true and fake photons have very different isolation distributions (see Fig. 2). Therefore, one expects different efficiencies for signal (true photons) and background (fake photons) for a given isolation cut. In a single-photon sample this property can be used to extract the number of true photons:

$$w = \sum_{i=1}^{N} \frac{\epsilon_i - \epsilon_b(E_{Ti})}{\epsilon_s(E_{Ti}) - \epsilon_b(E_{Ti})} \qquad (1)$$

where $\epsilon_i = 1$ if track-ISO < cut and $\epsilon_i = 0$ if track-ISO > cut, $\epsilon_s(E_T)$ is the signal efficiency for track-ISO < cut, $\epsilon_b(E_T)$ is the background efficiency for track-ISO < cut and N is the total number of candidate photons in the sample. This technique can be generalized in the case of the $\gamma\gamma$ sample and is based on a maximum likelihood approach, which is described in detail in Appendix A.

As mentioned in Sec. III, two types of isolation can be defined for central photons: calorimeter and track isolation. Cal-ISO is sensitive to the following contributions: underlying event (UE), multiple interactions, leakage from the photon cluster, and fragmentation contribution from jets (for fakes). Track-ISO, on the other hand, is only a measure of UE and fragmentation contribution. Therefore, it can potentially offer a better separation between true and fake photons. Using track-ISO for the fake photon background subtraction also has additional advantages that low-P_T tracks are very well measured (unlike the calorimeter energy) and jet fragmentation studies [27] indicate that track observables are well described by PYTHIA both for the UE and for the jets.

To perform the background subtraction, signal (ϵ_s) and background (ϵ_b) efficiencies are needed for a certain cut on track-ISO. The form of Eq. (1) suggests that the best accuracy in photon purity can be achieved when the absolute value of the denominator is maximum. When this happens, the terms in the sum of Eq. (1) are minimized in magnitude and thus the purity is less sensitive to the

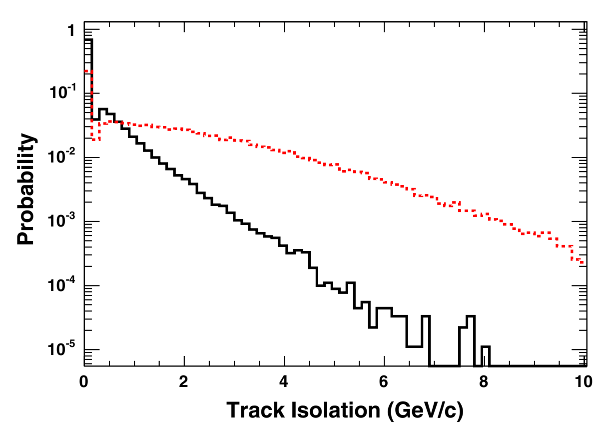

FIG. 2 (color online). The track-ISO distribution in signal (solid line) and background (dashed line) events.

statistical uncertainty of the number of events in the sample. Therefore, a scan of $\epsilon_s - \epsilon_b$ as a function of the track-ISO cut is performed using MC samples of true and fake photons. The difference peaks at track-ISO ~ 1 GeV. The threshold of the track-ISO cut for the signal and background efficiency functions is thus chosen at 1 GeV.

The signal track-ISO efficiency is obtained from PYTHIA photon-plus-jet samples. The background efficiency is obtained from PYTHIA dijet samples. All PYTHIA samples used in this work are derived from version 6.2.16 of the program using the CTEQ5L parton distribution functions (PDF) set for [28] and the "tune A" for UE parameters [29]. Background events are filtered out if a detector photon is matched to a generator level photon originating from quark ISR or FSR. This ensures that the background track-ISO efficiency function is obtained for neutral hadrons (mostly π^0 or η^0) faking a photon signature. Similarly, for the signal events, detector photons are required to match generator level photons from the hard scattering (thus fragmentation photons are removed). The signal efficiency ϵ_s and the background efficiency ϵ_b are shown in Fig. 3 as functions of the photon E_T. Both functions are parameterized by a linear combination of an exponential and a constant.

The isolation cones for the two photon candidates are not entirely independent. For example, if a particular event has a higher (lower) than average underlying event activity, then it is likely that both isolation cones will simultaneously have more (less) energy. In addition, the ordering in E_T of the two photons also introduces some bias. The signal (for $E_T < 50$ GeV) and the background track-ISO efficiencies drop with increasing E_T (see Fig. 3). Therefore, the lower E_T threshold for the first photon in the event relative to the second photon implies, on average, that the E_T of the first photon will be systematically lower than the E_T of the second photon, thus introducing some bias due to the E_T dependence of the efficiencies. This effect is negligible for $E_T > 50$ GeV, where the signal track-ISO efficiency is flat and the background is weak, but it becomes significant at low E_T. It is a small effect in the single-photon purity, but it is at least a factor of 2 more important for diphoton events. These correlations must be taken into account when calculating a probability of two photon candidates to pass-pass, pass-fail, fail-pass, or fail-fail the 1 GeV isolation cut described above. PYTHIA diphoton events were used to obtain "per event" track-ISO efficiencies for these combinations. Correlations are much less important for events with one or two fake photons because they are diluted by a much larger contribution from jet fragmentation.

The systematic uncertainties in the signal and background track-ISO efficiencies are estimated and propagated into the final estimate of photon purity. Correlations between different sources of systematics are taken into account. The following sources of uncertainties are considered: (1) mismodeling of the distribution of the number of vertices (N_{vx}) in MC (pile-up effect); (2) statistical uncertainties in the fit parameters; (3) choice of the fit function for the efficiency; (4) generator-related data–MC differences; (5) effect of the E_T threshold for selected photon candidates (only for the background). These uncertainties are presented in Fig. 4 and discussed below.

The MC simulation does not describe accurately the distribution of the number of reconstructed vertices. This effect can be either removed by reweighting the MC to match the data or the associated uncertainty can be assigned for the effect of mismodeling. The latter approach is chosen in this analysis because the track-ISO, to leading order, is not sensitive to the presence of multiple interactions and the effect is very small. This uncertainty is conservatively estimated as the difference between the extreme cases of track-ISO efficiencies obtained in events with $N_{vx} = 1$ and track-ISO efficiencies obtained in events with $N_{vx} > 1$. For the photon energies relevant to this analysis, the relative effect is $<1\%$ for the signal and $<3\%$ for the background.

The fit statistical uncertainties are included in the estimation of systematic uncertainties. Correlations between fit parameters are properly taken into account. The relative

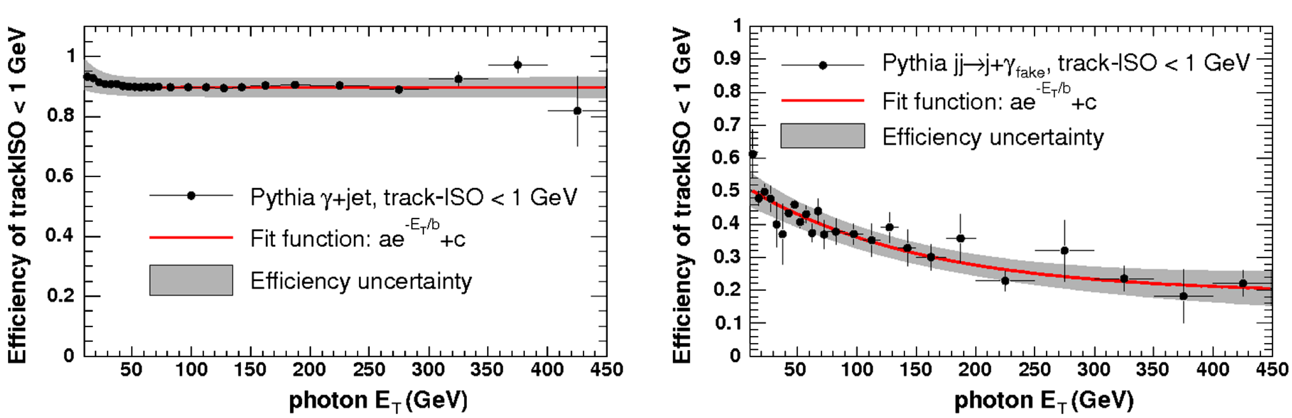

FIG. 3 (color online). Signal (left) and background (right) efficiencies for track-ISO < 1 GeV. The shaded area is the total systematic uncertainty.

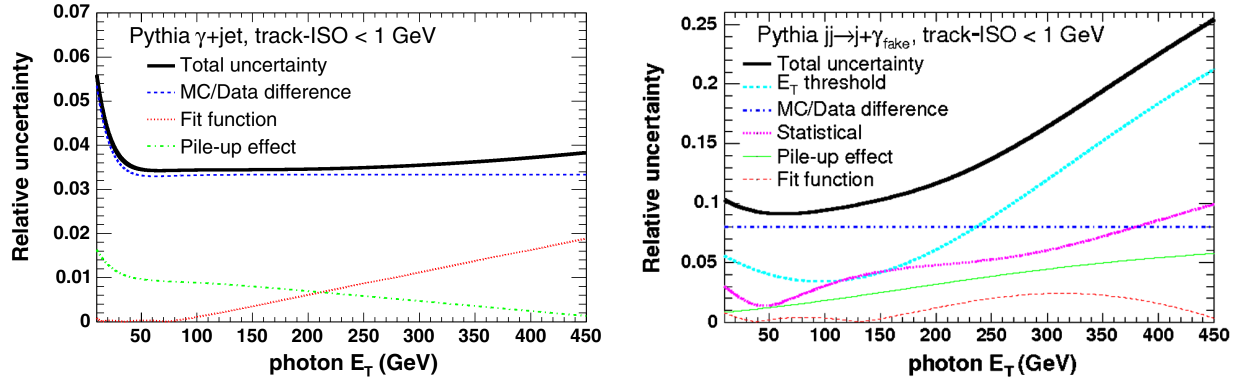

FIG. 4 (color online). Relative systematic uncertainties on the signal (left) and background (right) efficiencies for track-ISO < 1 GeV.

effect is negligible for the signal and 1%–3% for the background in the range of photon energies relevant to this analysis.

The default fit function choice is an exponential plus a constant term. As one can see from the track-ISO efficiency plots shown in Fig. 3, the quality of the fit is very good. The studies of the efficiency dependence on the track-ISO cut indicated that, for some cut values, the exponential plus a linear function can be a better fit to the signal efficiency. This function was thus chosen as an alternative track-ISO efficiency parameterization and the difference with the default function was taken as the associated uncertainty. The relative effect is $<1\%$ for both signal and background with $E_T < 200$ GeV.

The modeling of both signal and background relies on the MC. Therefore, it is necessary to assign a systematic uncertainty on possible data-MC differences both for signal and background photons. In the case of signal, it is necessary to check the modeling of the underlying event in the MC. This is done by means of complementary cones. The complementary cones are chosen such that their axes have the same angle θ with respect to the beam line as the photon candidate and are rotated by $\pm\pi/2$ in ϕ. These cones are assumed, on average, to collect the same amount of the underlying event as cones of the same size around true photons. This assumption is tested and confirmed in the MC. It is also checked that complementary cones for signal and background look very similar. Finally, the signal track-ISO efficiency is obtained from complementary cones in data and signal MC and the difference between the two is taken as the associated systematic uncertainty in the signal track-ISO efficiency. The comparison of track-ISO efficiencies for complementary cones in data, MC signal, and background is shown in Fig. 5. The relative effect is $\sim$3.5% for most of the photon energies. This is the largest systematic uncertainty for the signal track-ISO efficiency. The systematic uncertainty from this source decreases from 5.5% at $E_T = 10$ GeV to $\sim$3.5% at $E_T = 40$ GeV and then it stays at roughly the same level for $E_T > 40$ GeV. An additional uncertainty arises from the fact that the signal efficiency is derived from true photons generated only by direct $gq \to \gamma q$, $q\bar{q} \to \gamma g$, and $gg \to \gamma g$ production, omitting photons radiated from initial- or final-state quarks. Figure 6 shows that the track isolation of photons radiated from final-state quarks is somewhat different than that of photons produced by hard scattering or radiated from initial-state quarks. This difference is estimated to have a constant 2% effect on the signal track-ISO efficiency which is added to its total systematic uncertainty.

The systematic uncertainty due to data-MC differences in the track-ISO background efficiency is estimated by comparing the track-ISO cut efficiency for a leading track in dijet events from data and MC. This method assumes that jets with a leading neutral particle (e.g., π^0/η) have the same or very similar fragmentation properties as jets with a leading charged particle (e.g., $\pi^\pm$ or $K^\pm$). The following procedure is applied to both data and MC. Events with two well-balanced and back-to-back jets are used, satisfying $|E_T(\text{jet1}) - E_T(\text{jet2})|/[E_T(\text{jet1}) + E_T(\text{jet2})] < 0.3$ and $|\phi(\text{jet1}) - \phi(\text{jet2})| > 2.7$ rad. The event is rejected if there is a third jet with $E_T > 0.1 \times [E_T(\text{jet1}) + E_T(\text{jet2})]$. One of the jets (a probe jet) is

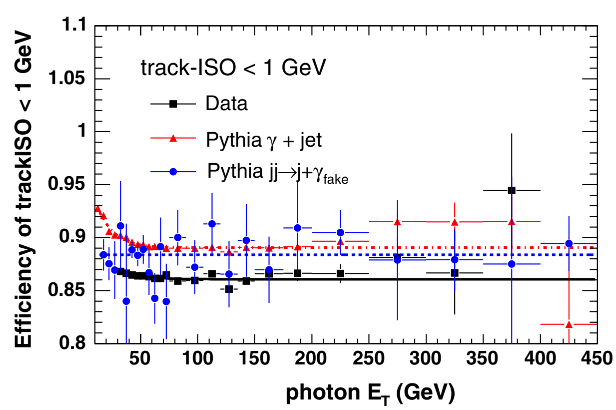

FIG. 5 (color online). Comparison of track-ISO < 1 GeV efficiencies in complementary cones from data (squares), signal MC (triangles), and background MC (circles).

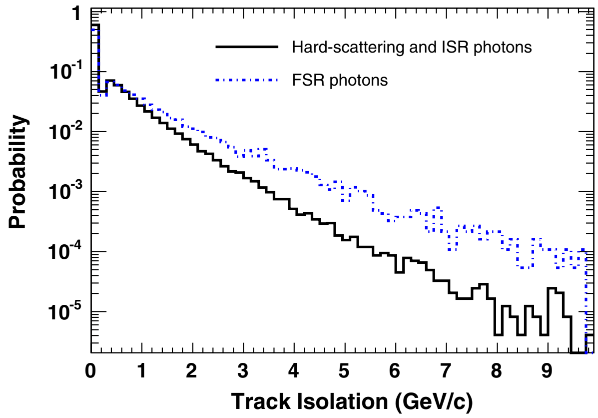

FIG. 6 (color online). The track-ISO distribution in hard scattering and ISR (dashed line) and FSR (solid line) events.

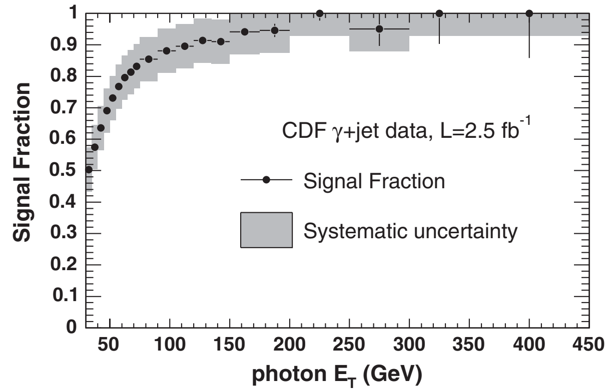

FIG. 7. The estimated signal fraction in the inclusive photon data. The shaded area is the total systematic uncertainty in the signal fraction.

required to be in the central detector region, $|\eta| < 1.1$, thus matching the pseudorapidity requirement for photons. In the next step, a well-reconstructed track (a probe track) is selected with the largest p_T inside the probe jet, i.e., inside a cone of $\Delta R = 0.4$ around the jet direction. For this track, an analog of the cal-ISO is calculated as the $\sum E_T$ of all towers inside a cone of $\Delta R = 0.4$ around the track direction. Towers associated with the track (up to 3 towers in η) are excluded from the sum. The cal-ISO for the probe track has to satisfy exactly the same requirements as the isolation for a photon with $E_T = p_T$. An analog of the track-ISO for the probe track is also calculated by following exactly the same procedure as for photons, with the only exception being that the track itself is excluded from the sum. Finally, the efficiency of the track-ISO < 1 GeV cut for the probe track is compared in data and MC. The observed relative difference of 8%, independent of the track p_T, is taken as an estimate of the systematic uncertainty due to data-MC differences in the track-ISO background efficiency.

Finally, the last source of systematic uncertainty in the background track-ISO efficiency is associated with the choice of an E_T threshold for selecting fake photons from a particular jet sample. The fake rate for jets is very small and, as a consequence, the MC dijet samples do not have enough statistics to yield a sufficient number of fake photons after the selection cuts. To maximize the statistics, fake photons are accepted from each dijet sample if $E_T > \hat{p}_T$ where $\hat{p}_T$ is the parton transverse momentum cutoff used in the event generation. Ideally, events with $E_T > (\hat{p}_T + \text{offset})$ should have been selected to avoid a bias due to the $\hat{p}_T$ threshold effect. This is necessary because fake photons carry, on the average, only 90% of the energy of the original parton. Therefore, the procedure is biased toward selecting fakes originating from gluon jets produced by radiation, which are not limited by the $\hat{p}_T$ threshold of hard scattering, and as a consequence toward lower background efficiencies. To obtain a conservative estimate of this effect, the threshold was lowered even more, thus accepting fake photons with $E_T > F \times \hat{p}_T$ where $F \sim 0.8$–0.9, depending on $\hat{p}_T$. By decreasing the threshold, the effect is overestimated, but this gives a conservative estimate of the associated uncertainty. The total systematic uncertainty of the background track-ISO efficiency is at the level of 10%–12% in the range of photon E_T from 15 to 200 GeV, the range relevant to this analysis.

The background subtraction procedure has been tested with MC signal and fake events as well as with inclusive photon data. Tests with MC provide closure checks: the returned purity was 100% for signal events and 0% for fakes (within the corresponding uncertainties). The estimated photon purity for inclusive photon data as a function of the photon transverse energy is shown in Fig. 7 and is similar to the purity obtained in the inclusive photon cross section analysis [10]. The uncertainty in the signal fraction of the inclusive photon sample achieved with the track-ISO method is between ~11% at low E_T and ~5% at very high E_T. Figure 8 shows the estimated purity for the diphoton data as a function of the kinematic variables defined in Sec. V B.

B. Event reconstruction and selection efficiency

The corrections for event reconstruction and selection efficiency were derived primarily from PYTHIA diphoton MC samples. The numerator of the efficiency is the number of events with two photons that pass all of the trigger criteria and selection cuts listed in Tables I and II. The definition of the cross section measurement is determined by the definition of the denominator of the efficiency. The denominator cuts are summarized in Table III. This work reports a cross section for isolated photons, so the selection of denominator events includes isolation. This isolation is found by summing over all generated hadrons and photons originating from the primary vertex within a cone of $\Delta R = 0.4$ around each photon.

For each kinematic quantity, one histogram of the reconstructed quantity and one of the quantity derived from

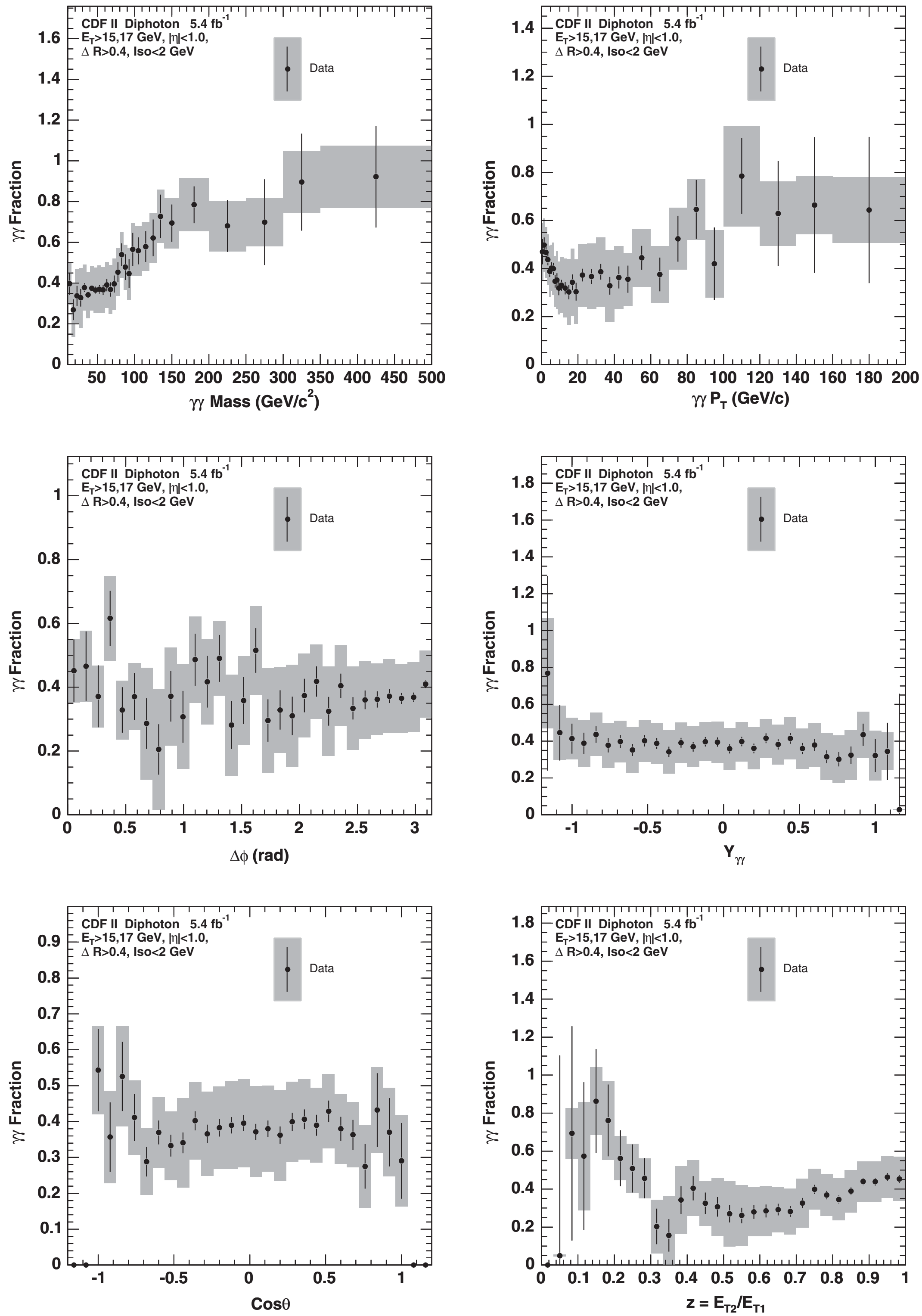

FIG. 8. The estimated signal fraction in the diphoton data as a function of several kinematic variables. The shaded area is the total systematic uncertainty in the signal fraction.

generator variables are constructed. In the first iteration, the efficiency is computed as the ratio of these histograms. This ratio also corrects event migration in neighboring bins due to finite resolution. Events which pass the denominator cuts and have a reconstructed value for the histogrammed quantity but not a generator level value are assigned the reconstructed values as the best approximation to the generator level values. To improve accuracy, the efficiency

TABLE III. Summary of the requirements applied to the generated MC events to define the denominator of the selection efficiency and the meaning of cross section measurement itself. y^γ is the photon rapidity [12].

Cuts	Selected $\gamma\gamma$ events
E_T^γ	≥ 15 GeV ($1^{st}\gamma$), ≥ 17 GeV ($2^{nd}\gamma$)
$\lvert y^\gamma \rvert$	≤ 1.0 for both photons
Isolation	≤ 2.0 GeV for both photons
$\Delta R(\gamma\gamma)$	≥ 0.4
	No matching requirement between generated and reconstructed objects

calculation is iterated a second time. Once all corrections are applied to the data, including the efficiency, it is the best available representation of the true distribution. Then the PYTHIA events are reweighted so that the second iteration of the denominator histogram agrees with the corrected data. The purpose is to correct the PYTHIA distribution closer to the true distribution, making the efficiency more accurate. In practice, this does not have a large effect on any distribution (see Fig. 9). A third iteration changes the efficiency at the level of 1% or less and, therefore, only two iterations are applied.

The following corrections are applied to the efficiency:

(i) $Z^0 \to e^+e^-$ events in data and MC are compared to derive a correction to the photon ID efficiency reported by the MC. The correction is reported as a function of N_{vx} and of run periods. The correction is weighted by the period luminosities, and the observed N_{vx} distributions to find an overall multiplicative efficiency correction of 0.967 per photon. In addition, there is some indication of an E_T-dependence, so the factor 0.967 is allowed to vary linearly up to 1.0 between 40 and 80 GeV, and then is held constant at 1.0 above 80 GeV.

(ii) A small correction is included near the E_T cut threshold due to the trigger turn-on curve. This is implemented as a factor of 0.98 at $E_T = 15$ GeV, going linearly up to 1.0 at $E_T = 18$ GeV. Ref. [10] concludes that there is no need for other corrections for the trigger.

(iii) PYTHIA includes the underlying event, but NLO calculations do not. This makes the PYTHIA-based efficiency correction too large when comparing the isolated cross section to NLO predictions. It is too large since the UE causes events to be removed from the isolated denominator of the efficiency. A correction is derived by convoluting the PYTHIA UE isolation energy with the DIPHOX energy in the isolation cone [6]. This reduces the probability for the DIPHOX event to pass the isolation cuts. This effect is measured to be a factor of 0.88 per event which is then applied as a correction to the data.

The efficiency obtained for the kinematic quantities defined in Sec. V B is shown in Fig. 9. The typical efficiency is 40%.

In addition to the total systematic uncertainty arising from the background subtraction, whose details are discussed in Sec. IV A, the following systematic uncertainties are included in the cross section measurement.

(i) The Z^0-based efficiency correction has an uncertainty from several sources, including uncertainty in the amount of material leading to conversion events, which are rejected, and the difference between the electron and photon response to cuts. These are summarized as 1.8% below $E_T = 40$ GeV, rising linearly to 3% at 80 GeV and fixed above that point. This increase completely covers the E_T-dependence in the photon ID efficiency mentioned above.

(ii) The photon energy scale is varied and the change in the kinematic distribution is reported as an uncertainty. For the diphoton mass, the variation is 0 at $E_T = 40$ GeV, rising linearly up to 1.5% at 80 GeV, then fixed above 80 GeV. These uncertainties are based on energy scale studies in the inclusive photon cross section measurement [30].

(iii) A 3% uncertainty due to trigger efficiency is taken from Ref. [10].

(iv) A 6% uncertainty (3% per photon) for underlying event correction is taken from Ref. [30].

(v) No uncertainty in the acceptance from variations in the ISR/FSR model is included since the primary mechanism for the effect is extra jets interfering with isolation. Both the numerator and denominator photons in the efficiency calculation are isolated, therefore the efficiency is immune to this effect, to leading order.

(vi) No uncertainty in the efficiency due to the choice of the Q^2 scale is included because the primary mechanism of this effect is through the boosting of the final state. Since the efficiency's numerator and denominator are calculated with full kinematic requirements, the efficiency is immune to this effect to leading order.

The breakdown of the systematic uncertainties for the kinematic quantities defined in Sec. V B is shown in Fig. 10. In all distributions, the dominant uncertainty comes from the background subtraction. The total systematic uncertainty is obtained by adding all individual components quadratically and averages near 30%.

C. Corrections and tests with the $Z^0 \to e^+e^-$ sample

The $Z^0 \to e^+e^-$ sample is used in this analysis for two purposes: (1) to set the energy scale in the central electromagnetic calorimeter and (2) to check the overall cross section normalization. The $Z^0 \to e^+e^-$ data sample is

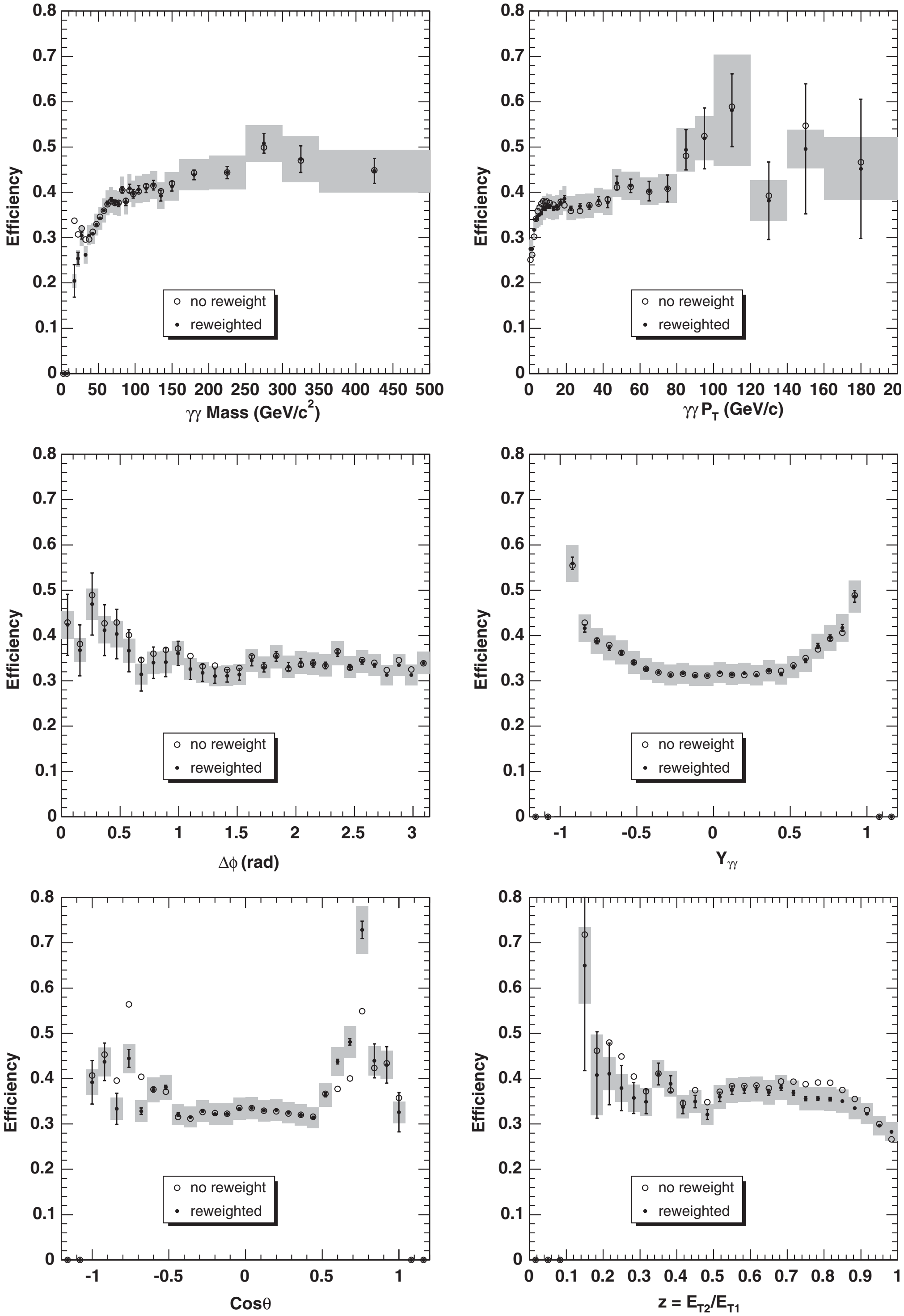

FIG. 9. The estimated efficiency as a function of several kinematic variables. The shaded area is the total systematic uncertainty in the efficiency.

derived from the diphoton trigger data set. The same global event selection as for the diphoton sample is applied. Two objects are required to pass a ''photonlike electron'' selection. The cuts applied are those of the standard photon selection, with modifications to allow for the electron track. The modifications are:

(i) The number of allowed tracks in the cluster is increased by 1.
(ii) The leading track p_T cut is applied on the second-highest p_T track instead of the highest one.
(iii) The track isolation is corrected by subtracting the leading track p_T.

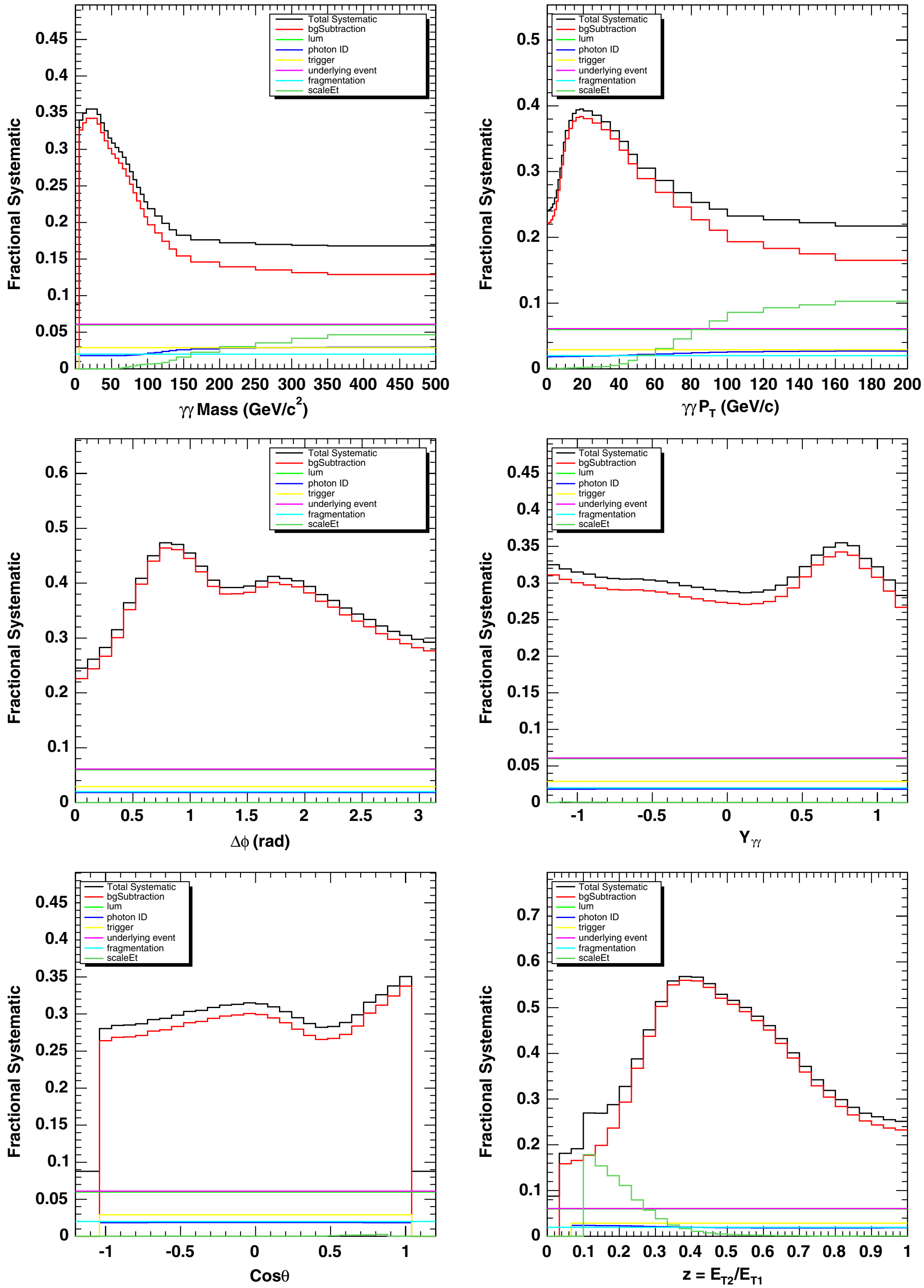

FIG. 10 (color online). The estimated systematic uncertainties in the cross section as a function of several kinematic variables.

(iv) $0.8 < E/p < 1.2$ is required for the energy-to-momentum ratio of the leading track. (Events which fail this cut also tend to fail the CES χ^2 cut.)

The electrons are required to match EM objects passing the Level 1 and Level 2 trigger criteria (or trigger simulation for the MC). A high-luminosity sample of fully simulated and reconstructed PYTHIA $Z^0 \rightarrow e^+e^-$ events is used for MC.

The electromagnetic energy scale is set by tuning the reconstructed Z^0 mass to the world average [13] in both the data and the MC samples. The correction is applied as a function of time. It is applied before final event selection to account for a few events slightly below the energy threshold which the correction pushes above the threshold. The correction can only have a noticeable effect on kinematic variables with rapidly falling spectra, related to the photon E_T, such as the diphoton mass. A 1.5% systematic uncertainty due to energy scale is included, as mentioned in Sec. IV B.

The $Z^0 \to e^+e^-$ cross section is measured in order to check the cross section measurement procedures. This measurement tests the trigger efficiency, the ability for the MC to predict the event selection efficiency, the efficiency corrections, and the luminosity. The cross section is measured for events with e^+e^- invariant mass between 65 and 115 GeV$/c^2$. The photonlike electron selection is applied and the efficiency from the PYTHIA MC is used. The same photon efficiency corrections as in the diphoton cross section (see Sec. IV B) are applied. Since the photonlike electron cuts are used, it is assumed that the response is similar to photon response. The resulting $Z^0 \to e^+e^-$ cross section is found to be consistent with previous dedicated measurements and expectation from theory [31].

V. RESULTS

This section presents the results of the cross section measurement. A brief description of the theoretical calculations is given first, then the comparisons for selected kinematic variables are shown and discussed. Tables with the measured cross section values are given in Appendix B.

A. Theoretical calculations

The results of this measurement are compared with three theoretical predictions:

(i) A calculation using the PYTHIA program [3]. This is a parton-showering generator which features a realistic representation of the physics events in terms of observable particles. It includes initial- and final-state radiation and an underlying event model. PYTHIA implements a leading-order (LO) matrix element (ME) for direct diphoton production which includes the $q\bar{q} \to \gamma\gamma$ and $gg \to \gamma\gamma$ LO processes described, respectively, by diagrams (a) and (b) of Fig. 1. Significant contributions also arise from the processes $q\bar{q} \to \gamma\gamma g$ (diagrams (c) of Fig. 1) and $gq \to \gamma\gamma q$ (diagrams (d) of Fig. 1) where the second photon is emitted from an initial- or final-state quark according to the PYTHIA radiation model. These contributions were included in the calculation by running the program with a filter selecting diphoton events from inclusive $\gamma + \mathrm{X}$ events, where X is either a photon or a jet, with an efficiency of 0.025%. Figure 11 shows the individual contributions to the cross section as a function of the diphoton invariant mass, transverse momentum, and azimuthal difference. Initial-state radiation (ISR) photons, in particular, produce substantially different distributions than ME and final-state radiation (FSR)

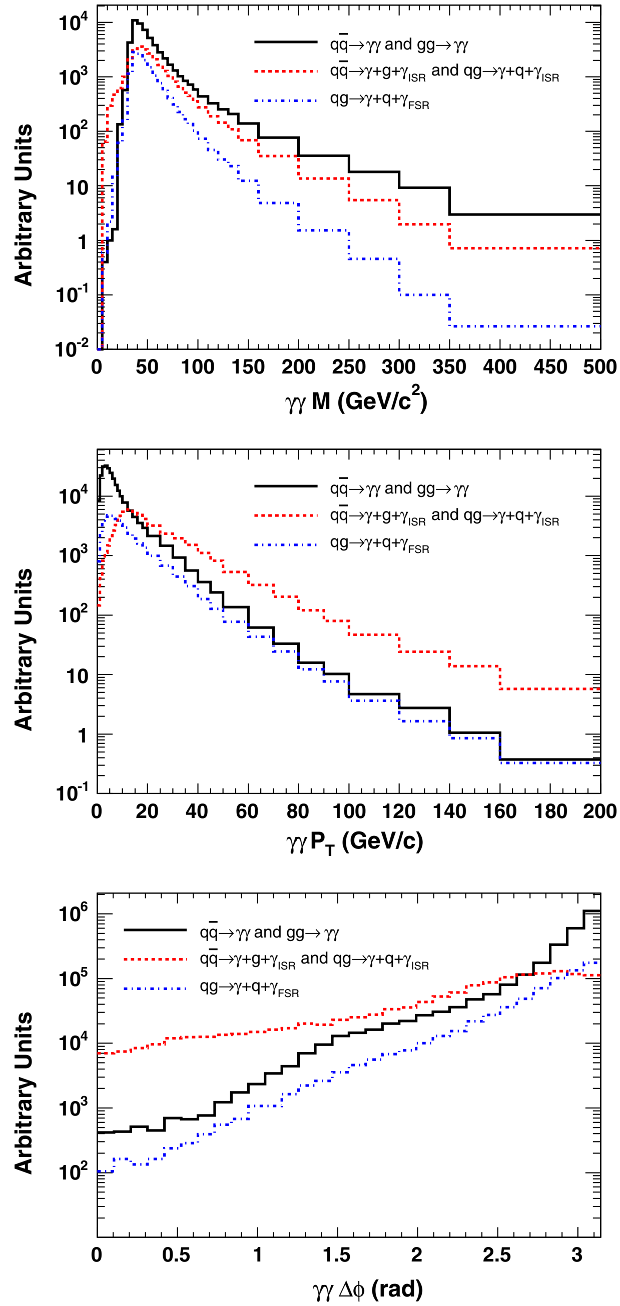

FIG. 11 (color online). The individual contributions to the cross section from events where both photons are generated according to the PYTHIA diphoton matrix element and from events where one photon originates from initial- or final-state radiation, as functions of the diphoton mass (top), transverse momentum (middle), and azimuthal difference (bottom).

photons, having a harder transverse momentum spectrum and stronger low-$\Delta\phi$ tail in the azimuthal difference spectrum. In leading order, this can be attributed to the fact that FSR occurs in quark-gluon scattering [diagram (d) of Fig. 1], whereas ISR occurs both in $q\bar{q}$ annihilation [diagram (c) of Fig. 1] and quark-gluon scattering, and the luminosity of quark-gluon states falls off more rapidly with the parton momenta than the luminosity of $q\bar{q}$ states [6,8]. The diphoton ME contributes 56% to the cross section, the processes $q\bar{q} \to g\gamma\gamma_{\rm ISR}$ and $gq \to q\gamma\gamma_{\rm ISR}$ 29%, and the process $gq \to q\gamma\gamma_{\rm FSR}$ 15%. Double radiation processes in minimum bias dijet events, such as $qq \to qq\gamma_{\rm ISR/FSR}\gamma_{\rm ISR/FSR}$, $q\bar{q} \to q\bar{q}\gamma_{\rm ISR/FSR}\gamma_{\rm ISR/FSR}$, $gq \to gq\gamma_{\rm ISR/FSR}\gamma_{\rm ISR/FSR}$, $q\bar{q} \to gg\gamma_{\rm ISR}\gamma_{\rm ISR}$ and $gg \to q\bar{q}\gamma_{\rm FSR}\gamma_{\rm FSR}$, were also examined but their overall contribution was estimated to only ~3% of the total, having no significant effect to any kinematical distribution. Therefore, these processes were not included in the PYTHIA calculation.

(ii) A fixed next-to-leading-order (NLO) calculation using the DIPHOX program [6]. This generator explicitly includes parton fragmentation into photons [9], *i.e.*, processes in which nearly all the energy of a parton is transformed into a photon. Direct production contributes 85% to the cross section and fragmentation 15%. The DIPHOX matrix element accounts for the $q\bar{q} \to \gamma\gamma$ and $gq \to \gamma\gamma q$ processes up to NLO, and LO for the $gg \to \gamma\gamma$ process, since this is already a second order process in the strong coupling. The NLO $gg \to \gamma\gamma$ contributions were examined with the GAMMA2MC program [7]. Figure 12 shows an example of the uncorrected and corrected DIPHOX predictions in comparison with the measured cross section as a function of the diphoton invariant mass M. The corrected prediction is calculated by running DIPHOX without the LO $gg \to \gamma\gamma$ term and then adding the full LO + NLO $gg \to \gamma\gamma$ calculation from GAMMA2MC incoherently, since the initial state is different in gluon fusion than in the other processes. The correction of the total cross section for the NLO $gg \to \gamma\gamma$ contribution is nearly 10%, which is comparable with the experimental and theoretical uncertainties (see Table IV). Therefore, this correction was not applied to the DIPHOX calculation.

(iii) A resummed NLO calculation using the RESBOS program [8]. Here the effects of soft gluon ISR in the NLO calculation are analytically resummed to all orders in the strong coupling and reach next-to-next-to-leading logarithmic (NNLL) accuracy. The resultant prediction is smoothly matched to the fixed-order NLO result in the kinematic regions where the NLO matrix element is dominant. The RESBOS matrix element includes the $q\bar{q} \to \gamma\gamma$, $gq \to \gamma\gamma q$, and $gg \to \gamma\gamma$ processes up to NLO and it is adjusted so as to approximately account for fragmentation.

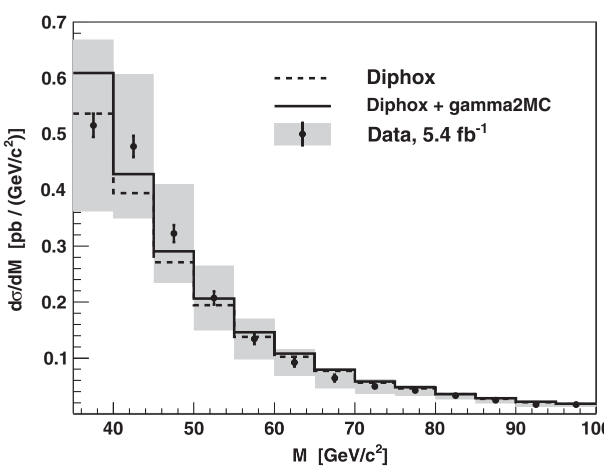

FIG. 12. The measured cross section as a function of the diphoton mass in comparison with the DIPHOX predictions without and with the NLO $gg \to \gamma\gamma$ correction, calculated by the GAMMA2MC program. The shaded area is the total systematic uncertainty in the data.

All calculations are done by Monte Carlo event generation and are subject to the experimental kinematic and isolation cuts. In the fixed-order NLO calculations, the isolation cut is applied on parton variables and thus it only approximates the isolation cut applied in the data and in PYTHIA. The RESBOS predictions are restricted in the diphoton invariant mass M range from $2m_b = 9$ GeV$/c^2$ to $2m_t = 350$ GeV$/c^2$ and they are shown up to $M = 300$ GeV$/c^2$ in the plots of the mass distribution, where m_b and m_t are the masses of the bottom and top quarks, respectively.

NLO theoretical uncertainties are estimated for the choice of scale, representing the sensitivity to missing higher order terms, and for the PDFs. In DIPHOX, the default renormalization, factorization, and fragmentation scales are all set to $\mu = M/2$. In RESBOS, the default renormalization and factorization scales are both set to $\mu = M$. In either case, all scales are varied by a factor of 2 up and down relative to the default choice and this is taken as a conservative estimate of the total scale uncertainty. The proton PDF set is the CTEQ6.1M set [32] for both DIPHOX and RESBOS. The corresponding uncertainty is estimated by varying the generated event weights within the 90% level uncertainties given by the 20 CTEQ6.1M eigenvectors.

TABLE IV. The total diphoton production cross section obtained from the measurement and from the theoretical calculations. The PYTHIA $\gamma\gamma$ calculation involves only the $q\bar{q} \to \gamma\gamma$ and $gg \to \gamma\gamma$ processes. The PYTHIA $\gamma\gamma + \gamma$j calculation includes also the $q\bar{q} \to \gamma\gamma g$ and $gq \to \gamma\gamma q$ processes.

	Cross section (pb)
Data	$12.47 \pm 0.21_{\rm stat} \pm 3.74_{\rm syst}$
RESBOS	$11.31 \pm 2.45_{\rm syst}$
DIPHOX	$10.58 \pm 0.55_{\rm syst}$
PYTHIA $\gamma\gamma + \gamma$j	9.19
PYTHIA $\gamma\gamma$	5.03

The measured total cross section is shown in Table IV together with the predictions from the three theoretical calculations. The three baseline calculations are consistent with the size of the measured cross section within the experimental uncertainties.

B. Kinematic variables

The complete description of the reaction $h_1 + h_2 \to \gamma_1 + \gamma_2 + X$, where $h_{1,2}$ are hadrons, requires five independent kinematic variables. A suitable choice consists of the invariant mass

$$M = \sqrt{2p_{T\gamma 1}p_{T\gamma 2}[\cosh(y_{\gamma 1} - y_{\gamma 2}) - \cos(\phi_{\gamma 1} - \phi_{\gamma 2})]}, \tag{2}$$

the transverse momentum

$$P_T = \sqrt{p_{T\gamma 1}^2 + p_{T\gamma 2}^2 + 2p_{T\gamma 1}p_{T\gamma 2}\cos(\phi_{\gamma 1} - \phi_{\gamma 2})}, \tag{3}$$

the rapidity

$$Y_{\gamma\gamma} = \tanh^{-1}\frac{p_{T\gamma 1}\sinh y_{\gamma 1} + p_{T\gamma 2}\sinh y_{\gamma 2}}{p_{T\gamma 1}\cosh y_{\gamma 1} + p_{T\gamma 2}\cosh y_{\gamma 2}}, \tag{4}$$

and the azimuthal difference

$$\Delta\phi = |\phi_{\gamma 1} - \phi_{\gamma 2}| \bmod \pi \tag{5}$$

of the photon pair in the laboratory frame [12], and the cosine of the polar angle θ of the 1st photon in the Collins-Soper frame [33]. This is defined as the rest frame of the photon pair chosen so that (a) the 3-momenta $\vec{p}_{h_1}$ and $\vec{p}_{h_2}$ of the initial hadrons lie in the Oxz plane (with positive x) and (b) the z axis bisects the angle between $\vec{p}_{h_1}$ and $-\vec{p}_{h_2}$. This variable is generally determined by [33]

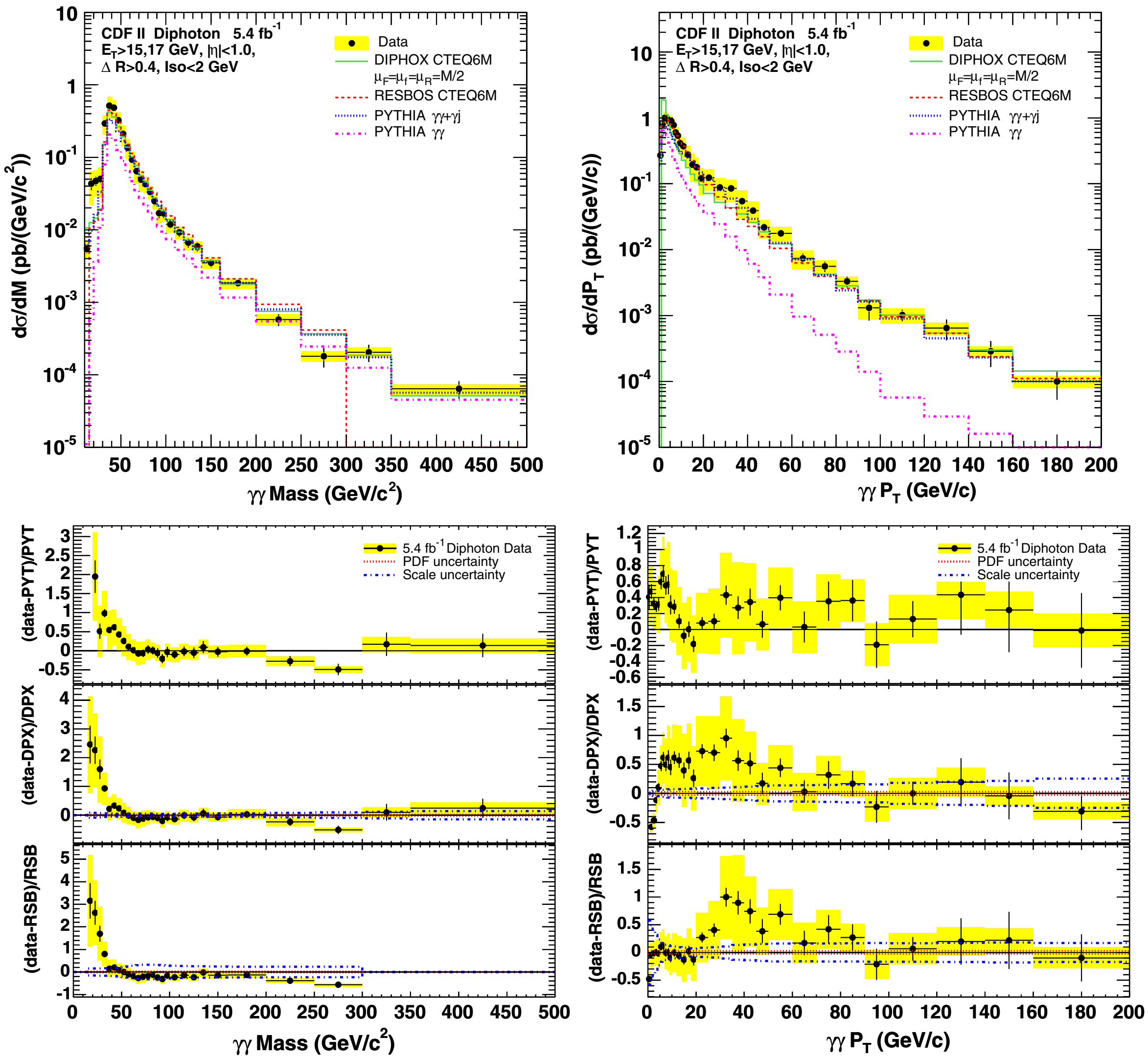

FIG. 13 (color online). The cross section as a function of the diphoton invariant mass (left) and transverse momentum (right). *Top:* the absolute cross section values. *Bottom:* the relative deviations of the data from the predictions. *Note:* the vertical axes scales differ between relative deviation plots. The shaded area is the total systematic uncertainty in the data.

$$\cos\theta = \frac{2p_{T\gamma1}p_{T\gamma2}\sinh(y_{\gamma1} - y_{\gamma2})}{M\sqrt{M^2 + P_T^2}}. \quad (6)$$

For photons emitted at large angles with respect to the beam, $\cos\theta \approx \tanh[(y_{\gamma1} - y_{\gamma2})/2]$ in the limit $P_T \to 0$. In the above equations, $p_{T\gamma i}$, $y_{\gamma i}$, and $\phi_{\gamma i}$ are the transverse momentum, rapidity, and azimuth of photon i, respectively, with $i = 1, 2$.

The set of $\{M, P_T, Y_{\gamma\gamma}\}$ describes the kinematics of the diphoton system and, therefore, of possible heavy particles decaying into a photon pair, such as a Higgs boson. The existence of such a particle would manifest as a peak in the distribution of the invariant mass M. The results of this analysis are presented in the form of cross sections differential in each of the five kinematic variables $\{M, P_T, \Delta\phi, Y_{\gamma\gamma}, \cos\theta\}$ and in the variable $z = p_{T\gamma2}/p_{T\gamma1}$, the ratio of subleading to leading photon transverse momentum ($0 \leq z \leq 1$). Three kinematic cases are examined:

(i) Differential cross sections without additional kinematic cuts. No kinematic cut other than those listed in Table III is applied. The results of this case are presented in Sec. V C.

(ii) Differential cross sections for $P_T < M$. The kinematics in this case are similar to the diphoton decay of a heavy particle, such as a Higgs boson, produced in events of moderate parton activity. At the Tevatron, prompt photon pairs are almost entirely produced in this case by low-P_T quark-antiquark

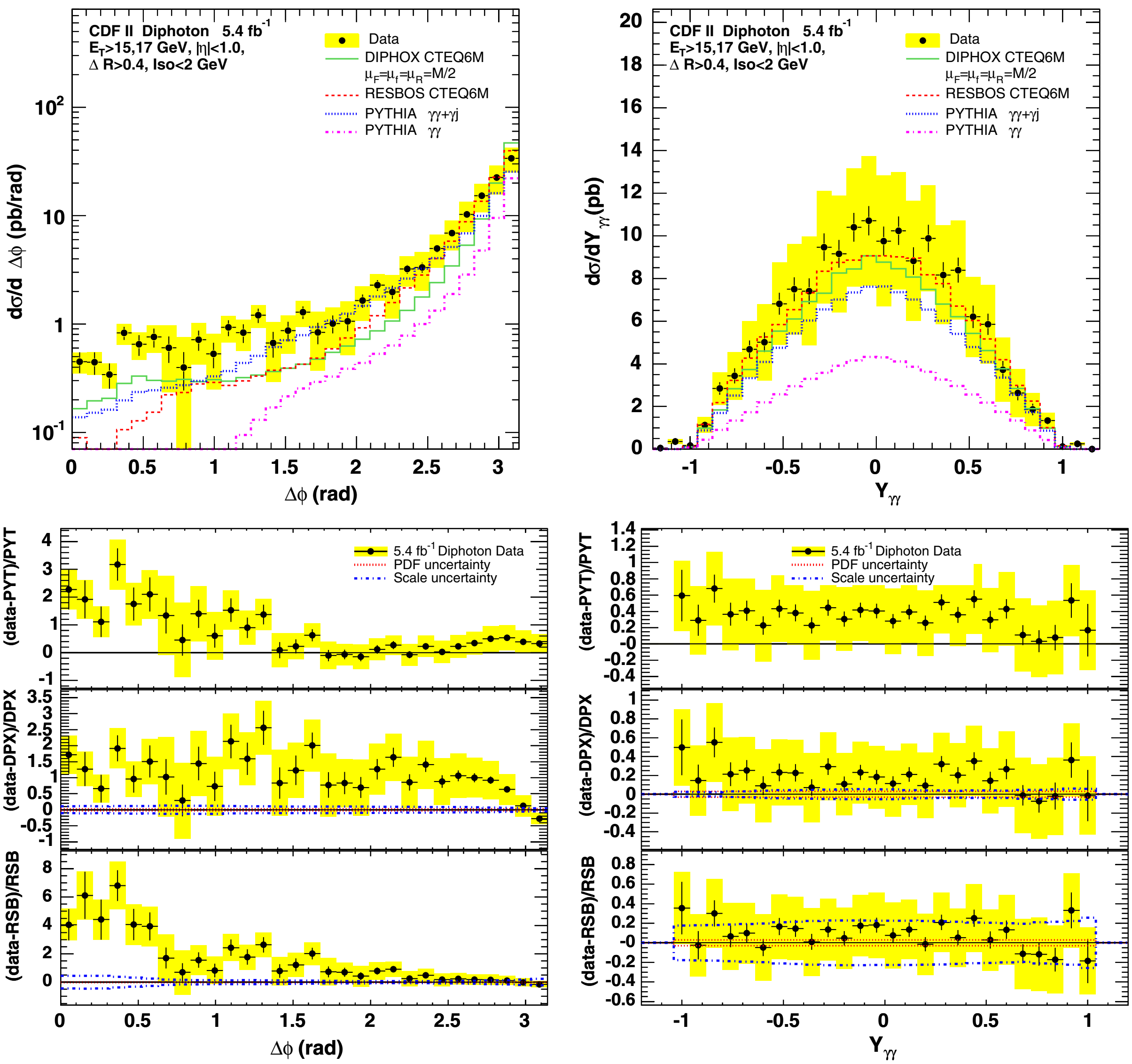

FIG. 14 (color online). The cross section as a function of the diphoton azimuthal distance (left) and of the diphoton rapidity (right). *Top:* the absolute cross section values. *Bottom:* the relative deviations of the data from the predictions. *Note:* the vertical axes scales differ between relative deviation plots. The shaded area is the total systematic uncertainty in the data.

annihilation. The results of this case are presented in Sec. V D.

(iii) Differential cross sections for $P_T > M$. The importance of high-P_T contributions from gluon-gluon fusion, fragmentations, and ISR is enhanced in this case. The results of this case are presented in Sec. V E.

The overflow data entries are excluded from the M and P_T histograms, to keep the cross section definition consistent for the data and the theories at the highest bins. For each kinematic variable, the following plots are presented:

(i) The measured and calculated cross sections as functions of the selected variable. Each of these plots includes the predictions of all three calculations, for comparison, and shows only the uncertainties of the data. The prediction of the PYTHIA $\gamma\gamma$ calculation, involving only the $q\bar{q} \to \gamma\gamma$ and $gg \to \gamma\gamma$ processes, is also shown in these plots, to be compared with the PYTHIA $\gamma\gamma + \gamma j$ calculation ($j =$ jet), which includes also the $q\bar{q} \to \gamma\gamma g$ and $gq \to \gamma\gamma q$ processes.

(ii) The relative deviations of the data from each calculation, in the form (data–theory)/theory, as functions of the selected variable. These plots show the comparison of the data with each calculation separately and include the uncertainties of the NLO

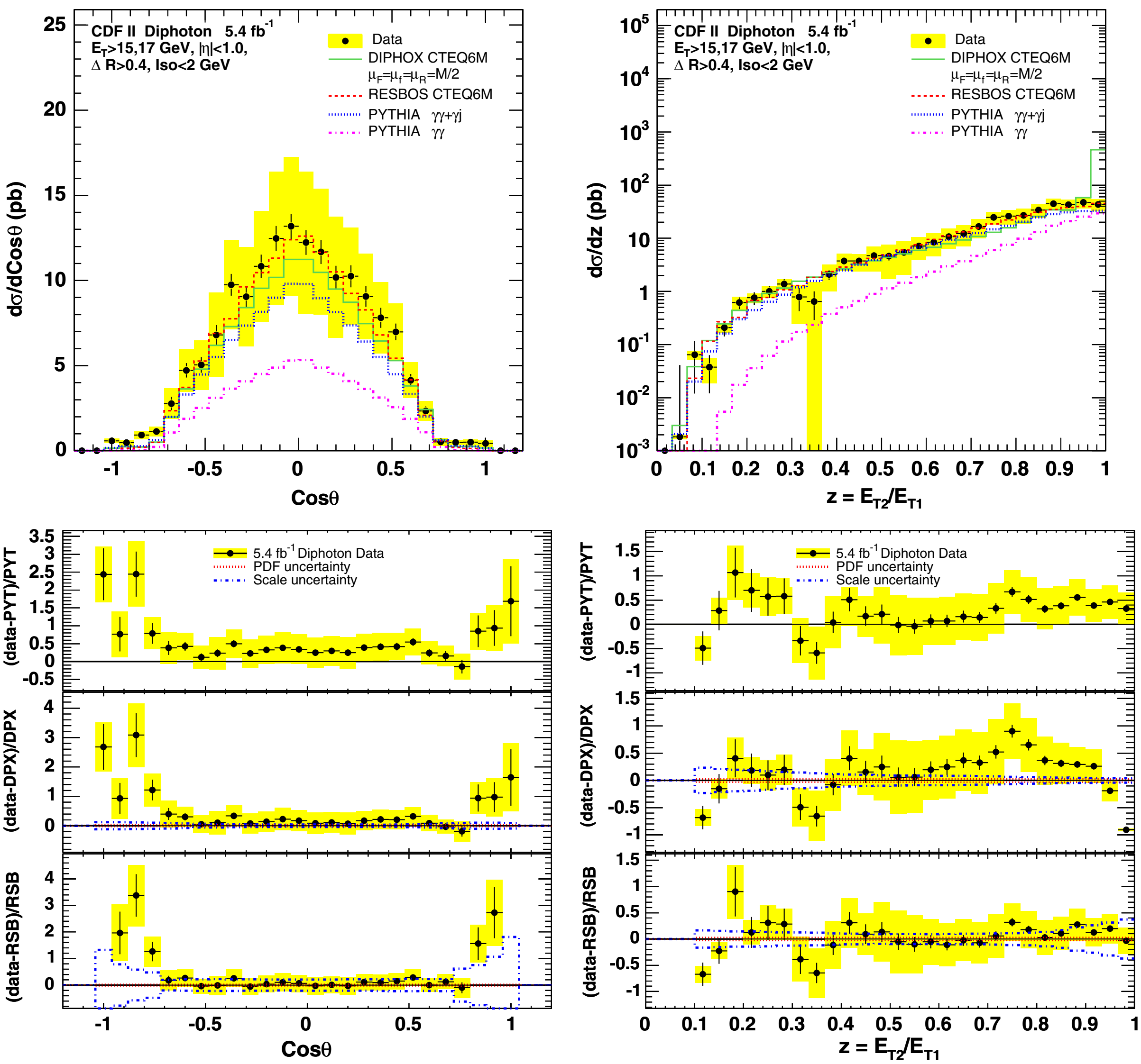

FIG. 15 (color online). The cross section as a function of the cosine of the polar angle in the Collins-Soper frame (left) and of the ratio of the subleading photon E_T to leading photon E_T (right). *Top:* the absolute cross section values. *Bottom:* the relative deviations of the data from the predictions. *Note:* the vertical axes scales differ between relative deviation plots. The shaded area is the total systematic uncertainty in the data.

predictions. No relative deviations are shown for the PYTHIA $\gamma\gamma$ calculation. The benchmark parton showering MC calculation, compared in detail with the data, is PYTHIA $\gamma\gamma + \gamma j$.

C. Differential cross sections without additional kinematic cut

Figure 13 shows the results for $d\sigma/dM$ and $d\sigma/dP_T$. The mass spectrum peaks at $M = 2\sqrt{E_{T1}^{\min}E_{T2}^{\min}} \approx 32\ \mathrm{GeV}/c^2$. All three theoretical predictions for $d\sigma/dM$ are in reasonable agreement with the data, within uncertainties, except in the region $6\ \mathrm{GeV}/c^2 < M < 32\ \mathrm{GeV}/c^2$ below the mass peak. The low mass limit of $6\ \mathrm{GeV}/c^2$ is set by the $\Delta R(\gamma\gamma)$ and E_T^{γ} cuts. This region is rich in events coming from gluon scattering and fragmentation. All three predictions underestimate the data in this region.

The excess of the data over all three predictions for M below the peak of the mass spectrum is reflected in the region $20\ \mathrm{GeV}/c < P_T < 50\ \mathrm{GeV}/c$ of the P_T spectrum, which has a shoulder around $P_T = p_{T2}^{\min} + p_{T1}^{\min} = 32\ \mathrm{GeV}/c$ (the so-called "Guillet shoulder"). This arises from a collinear enhancement for the two photons in the fragmentation processes which, however, is suppressed by the $\Delta R(\gamma\gamma)$ cut. The RESBOS predictions

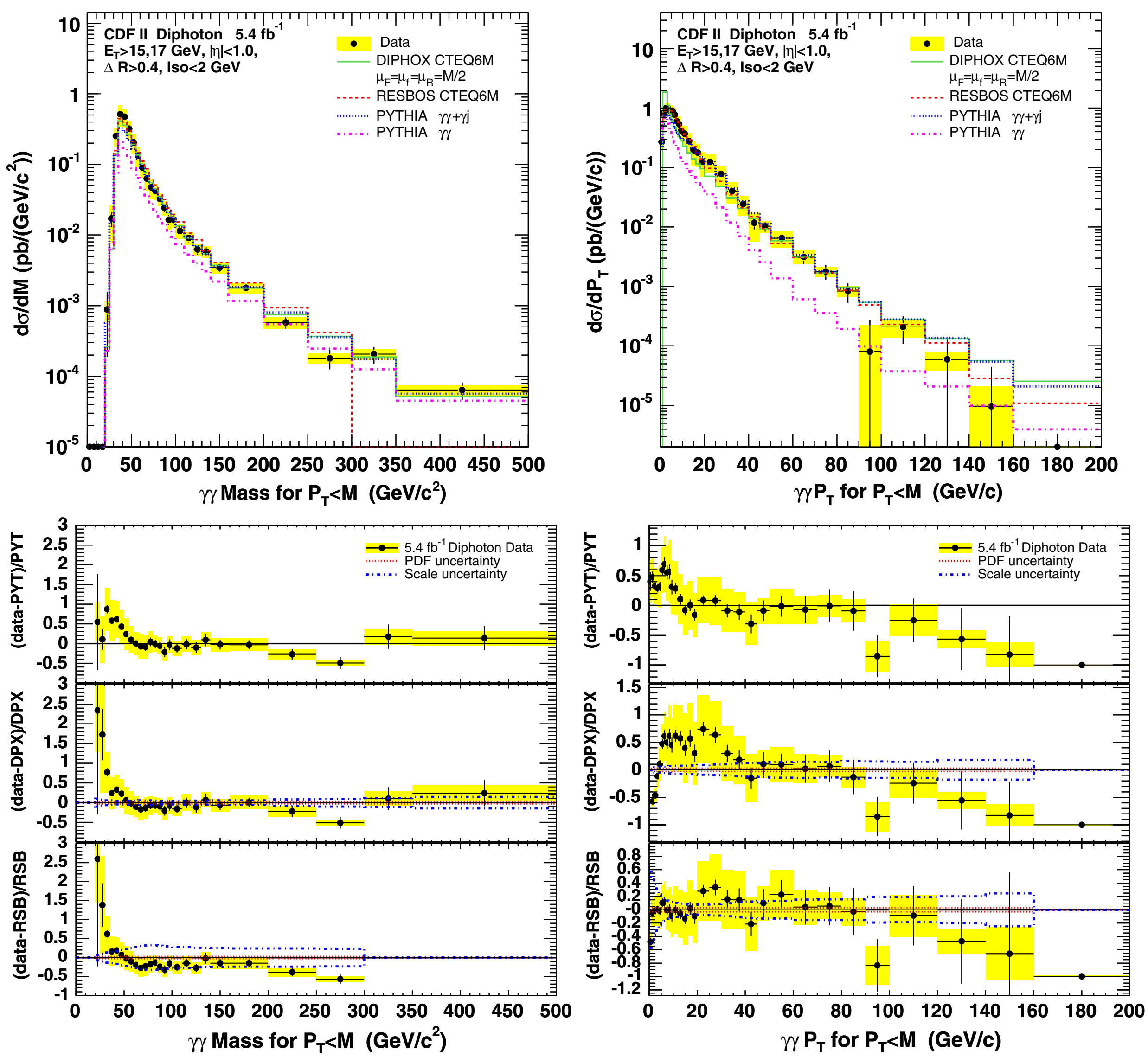

FIG. 16 (color online). The cross section as a function of the diphoton invariant mass (left) and transverse momentum (right) for $P_T < M$. *Top:* the absolute cross section values. *Bottom:* the relative deviations of the data from the predictions. *Note:* the vertical axes scales differ between relative deviation plots. The shaded area is the total systematic uncertainty in the data.

for $d\sigma/dP_{\mathrm{T}}$ are in overall agreement with the data, within uncertainties, except in this region. The DIPHOX prediction underestimates the data, in addition, for $P_{\mathrm{T}} < 20$ GeV/c, where the resummation effects implemented in RESBOS provide a better description. The PYTHIA prediction underestimates the data at very low P_{T}, $P_{\mathrm{T}} < 10$ GeV/c, showing that the LL resummation of parton showering is less accurate than the NNLL resummation implemented in RESBOS. The PYTHIA prediction is in reasonably good agreement with the data, within uncertainties, in the rest of the P_{T} range due to the $q\bar{q} \to g\gamma\gamma_{\mathrm{ISR}}$ and $gq \to q\gamma\gamma_{\mathrm{ISR}}$ processes which make the PYTHIA P_{T} spectrum sufficiently hard (see the middle plot of Fig. 11).

Figure 14 shows the results for $d\sigma/d\Delta\phi$ and $d\sigma/dY_{\gamma\gamma}$. The $\Delta\phi$ spectrum peaks at $\Delta\phi = \pi$, corresponding to vanishing diphoton P_{T}, and the $Y_{\gamma\gamma}$ spectrum at $Y_{\gamma\gamma} = 0$, corresponding to vanishing diphoton momentum P_z parallel to the proton beam. While all three predictions agree fairly well with the measured $d\sigma/dY_{\gamma\gamma}$, within uncertainties, all three of them underestimate the data in the low end of the $\Delta\phi$ spectrum. This region is dominated by events with low mass and high P_{T}. The RESBOS prediction provides the best description of the measured $d\sigma/d\Delta\phi$ for $\Delta\phi > 2.5$ rad, where soft gluon resummation is important. PYTHIA provides the best description in the region 1 rad $<$ $\Delta\phi < 2.5$ rad where the $q\bar{q} \to g\gamma\gamma_{\mathrm{ISR}}$ and $gq \to q\gamma\gamma_{\mathrm{ISR}}$

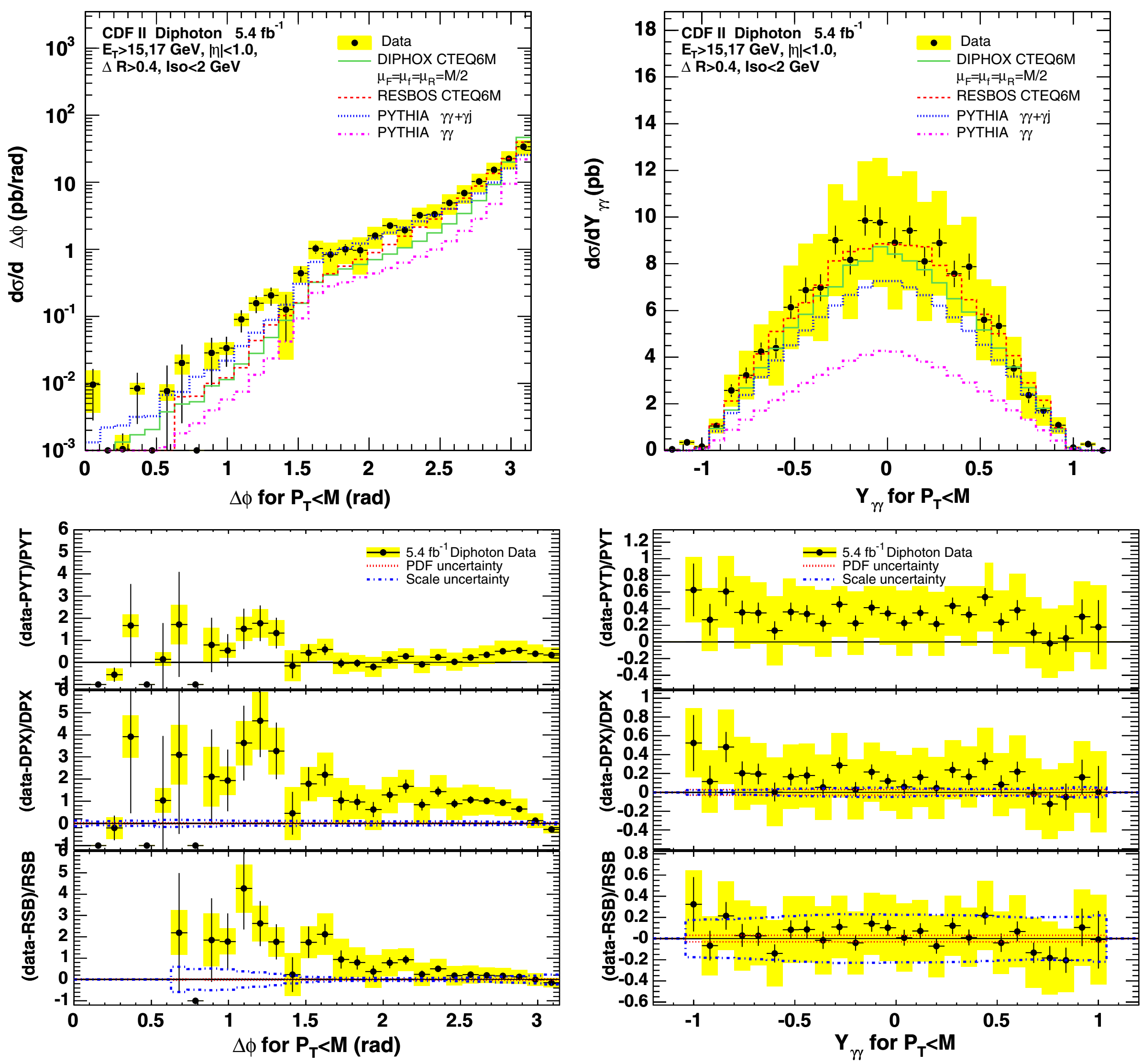

FIG. 17 (color online). The cross section as a function of the diphoton azimuthal distance (left) and of the diphoton rapidity (right) for $P_{\mathrm{T}} < M$. *Top:* the absolute cross section values. *Bottom:* the relative deviations of the data from the predictions. *Note:* the vertical axes scales differ between relative deviation plots. The shaded area is the total systematic uncertainty in the data.

processes are the most important (see the bottom plot of Fig. 11).

Figure 15 shows the results for $d\sigma/d\cos\theta$ and $d\sigma/dz$. All three predictions agree with the data, within uncertainties. Exceptions are the predictions of all three calculations underestimating the data in the two ends of the $\cos\theta$ spectrum, where again gluon scattering processes and associated fragmentation are expected to dominate [8].

In general, all three calculations reproduce most of the main features of the data, as observed in the earlier diphoton cross section measurements [10,11]. However, depending on their approximations, they display differences with each other and with the data in certain kinematic regions. There is a problem common to all three calculations in the description of events with very low diphoton mass, low azimuthal distance, and diphoton transverse momentum in the region of the Guillet shoulder. Such events include fragmentation at a relatively high rate. The PYTHIA $\gamma\gamma$ calculation fails completely to describe the data both in the scale, where it is low by a factor of 2.5, and in the shape, particularly of the P_T, $\Delta\phi$, and z distributions, where it predicts a much softer spectrum than the data. This is in agreement with the conclusion of Ref. [10] which tested only PYTHIA $\gamma\gamma$ as a parton showering MC prediction.

D. Differential cross sections for $P_T < M$ kinematics

Figure 16 shows the results for $d\sigma/dM$ and $d\sigma/dP_T$ for $P_T < M$. The low tail of the mass spectrum, in the region

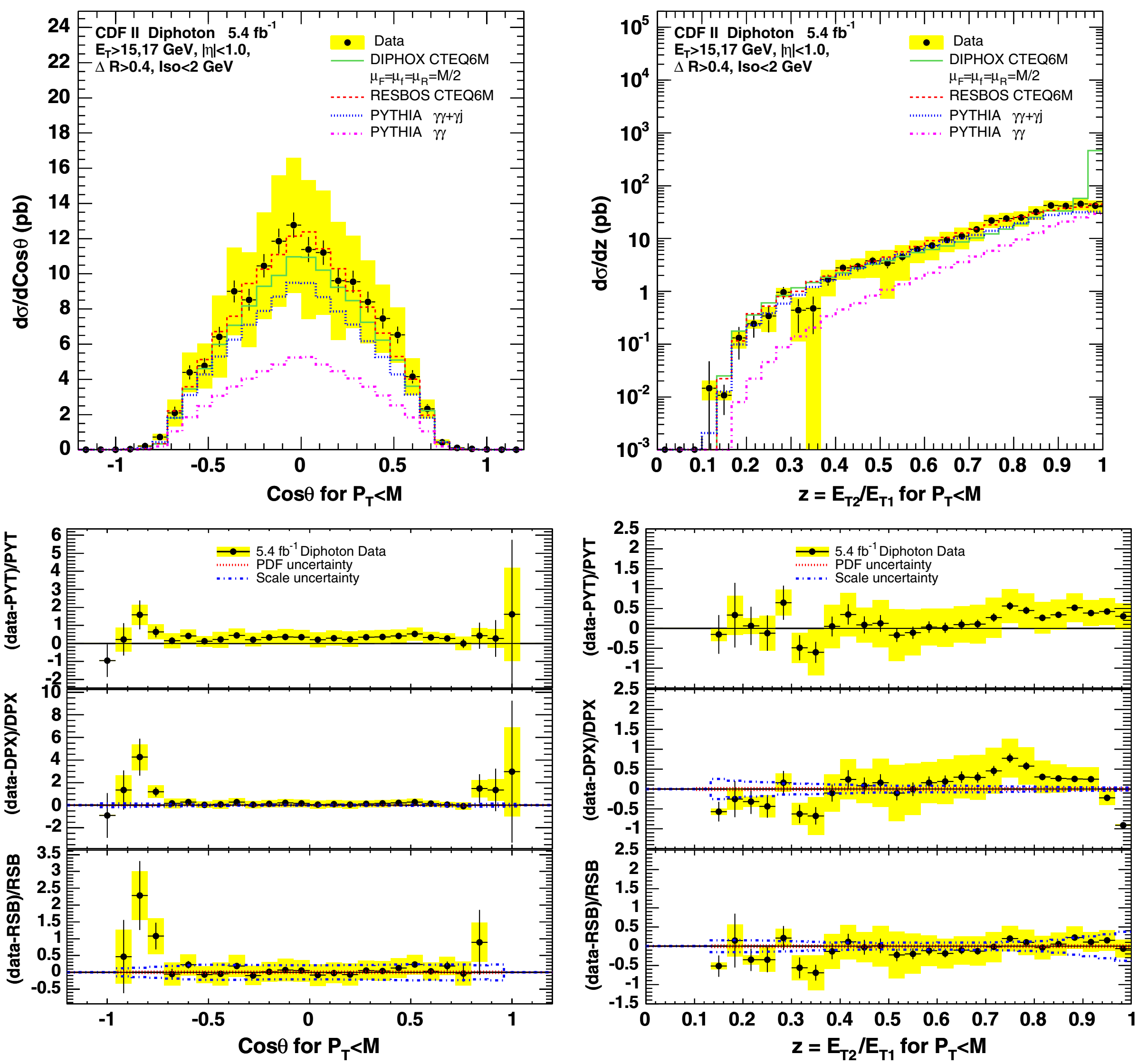

FIG. 18 (color online). The cross section as a function of the cosine of the polar angle in the Collins-Soper frame (left) and of the ratio of the subleading photon E_T to leading photon E_T (right) for $P_T < M$. *Top:* the absolute cross section values. *Bottom:* the relative deviations of the data from the predictions. *Note:* the vertical axes scales differ between relative deviation plots. The shaded area is the total systematic uncertainty in the data.

$6\ \mathrm{GeV}/c^2 < M < 32\ \mathrm{GeV}/c^2$, and the shoulder of the P_T spectrum, in the region $20\ \mathrm{GeV}/c < P_\mathrm{T} < 50\ \mathrm{GeV}/c$, are now eliminated. The agreement between the data and all three predictions is improved in this case. However, DIPHOX still underestimates the data for $P_\mathrm{T} < 40\ \mathrm{GeV}/c$ and similarly PYTHIA still underestimates the data for $P_\mathrm{T} < 10\ \mathrm{GeV}/c$, thus showing the importance of NNLL low-P_T resummation in this case as well.

Figure 17 shows the results for $d\sigma/d\Delta\phi$ and $d\sigma/dY_{\gamma\gamma}$ for $P_\mathrm{T} < M$. The tail of the $\Delta\phi$ spectrum for $\Delta\phi < \pi/2$ is now weaker but the measured cross section is underestimated by all three predictions, as in the case of unconstrained kinematics.

Figure 18 shows the results for $d\sigma/d\cos\theta$ and $d\sigma/dz$ for $P_\mathrm{T} < M$. The results are similar to the case of unconstrained kinematics. Generally, all three calculations agree with the data, within uncertainties. Exceptions are again the predictions of all three calculations in the two ends of the $\cos\theta$ spectrum, where they underestimate the data.

In general, events with kinematics similar to the decay of a heavy particle with low transverse momentum into a photon pair, such as $gg \to H \to \gamma\gamma$ production and decay, are better described by the theory than events with low mass and high transverse momentum. This is also observed in Ref. [11] which examines only the case of $P_\mathrm{T} < M$. This observation is important for current searches of yet undiscovered particles with a diphoton decay signature. The PYTHIA $\gamma\gamma$ calculation again fails to describe the data both in the scale and in the shape,

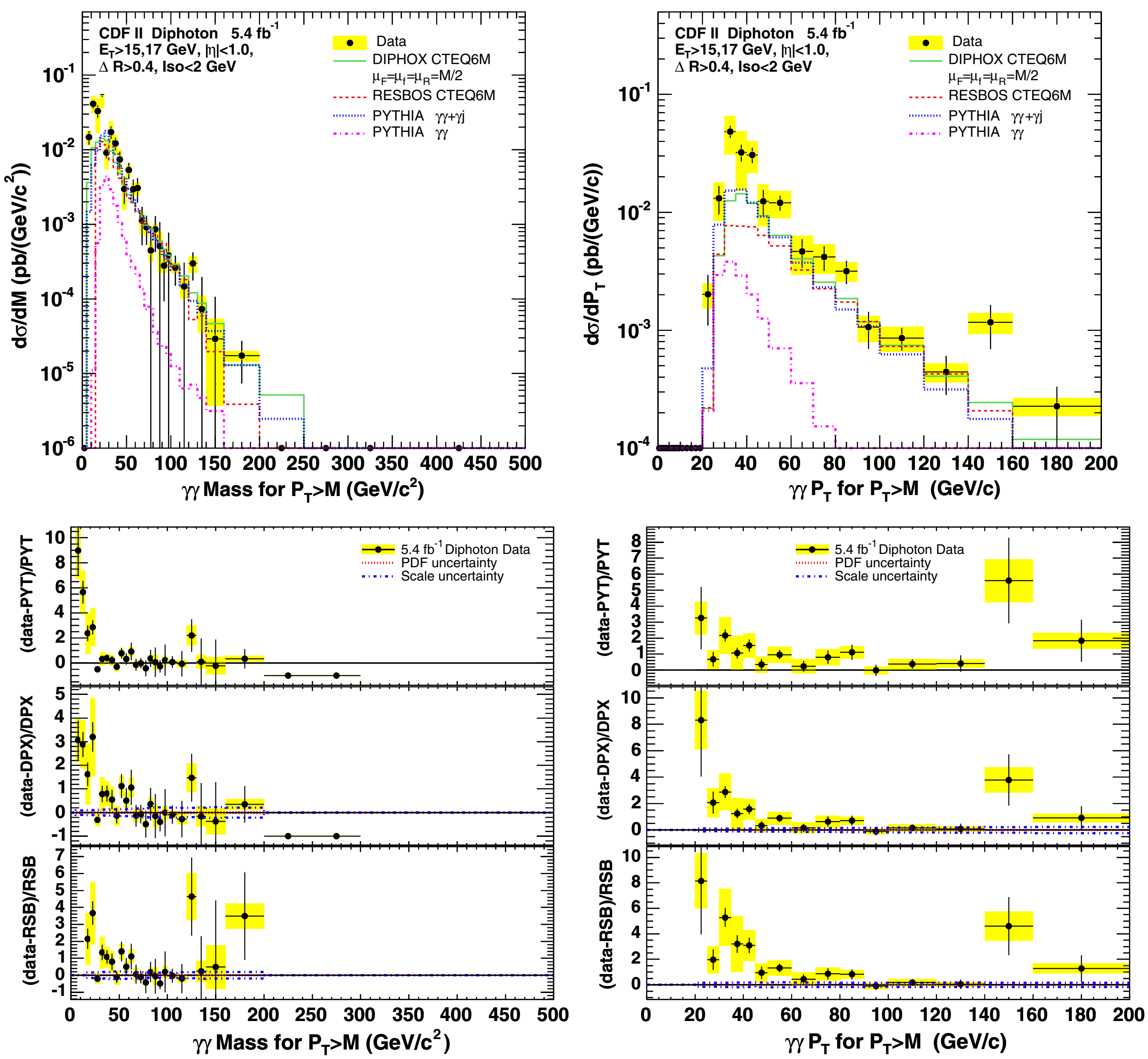

FIG. 19 (color online). The cross section as a function of the diphoton invariant mass (left) and transverse momentum (right) for $P_\mathrm{T} > M$. *Top:* the absolute cross section values. *Bottom:* the relative deviations of the data from the predictions. *Note:* the vertical axes scales differ between relative deviation plots. The shaded area is the total systematic uncertainty in the data.

in agreement with the conclusion of Ref. [11] which tested only PYTHIA $\gamma\gamma$ as a parton showering MC prediction.

E. Differential cross sections for $P_T > M$ kinematics

Figure 19 shows the results for $d\sigma/dM$ and $d\sigma/dP_T$ for $P_T > M$. Both spectra are depleted in this case: the mass spectrum for $M > 200\ \mathrm{GeV}/c^2$ and the transverse momentum spectrum for $P_T < 20\ \mathrm{GeV}/c$. All three calculations underestimate the data.

Figure 20 shows the results for $d\sigma/d\Delta\phi$ and $d\sigma/dY_{\gamma\gamma}$ for $P_T > M$. The $\Delta\phi$ spectrum is strongly suppressed for $\Delta\phi > \pi/2$. Again, the measured cross section is underestimated by all three calculations.

Figure 21 shows the results for $d\sigma/d\cos\theta$ and $d\sigma/dz$ for $P_T > M$. In contrast with the unconstrained kinematics and the $P_T < M$ kinematics, in this case all three calculations underestimate the data through the full ranges of the $\cos\theta$ and z spectra.

In general, events with low diphoton mass and high diphoton transverse momentum, mainly coming from fragmentation, are not well described by the examined calculations. This observation is important for measurements under conditions where contributions from such events are strong, as in the LHC [1].

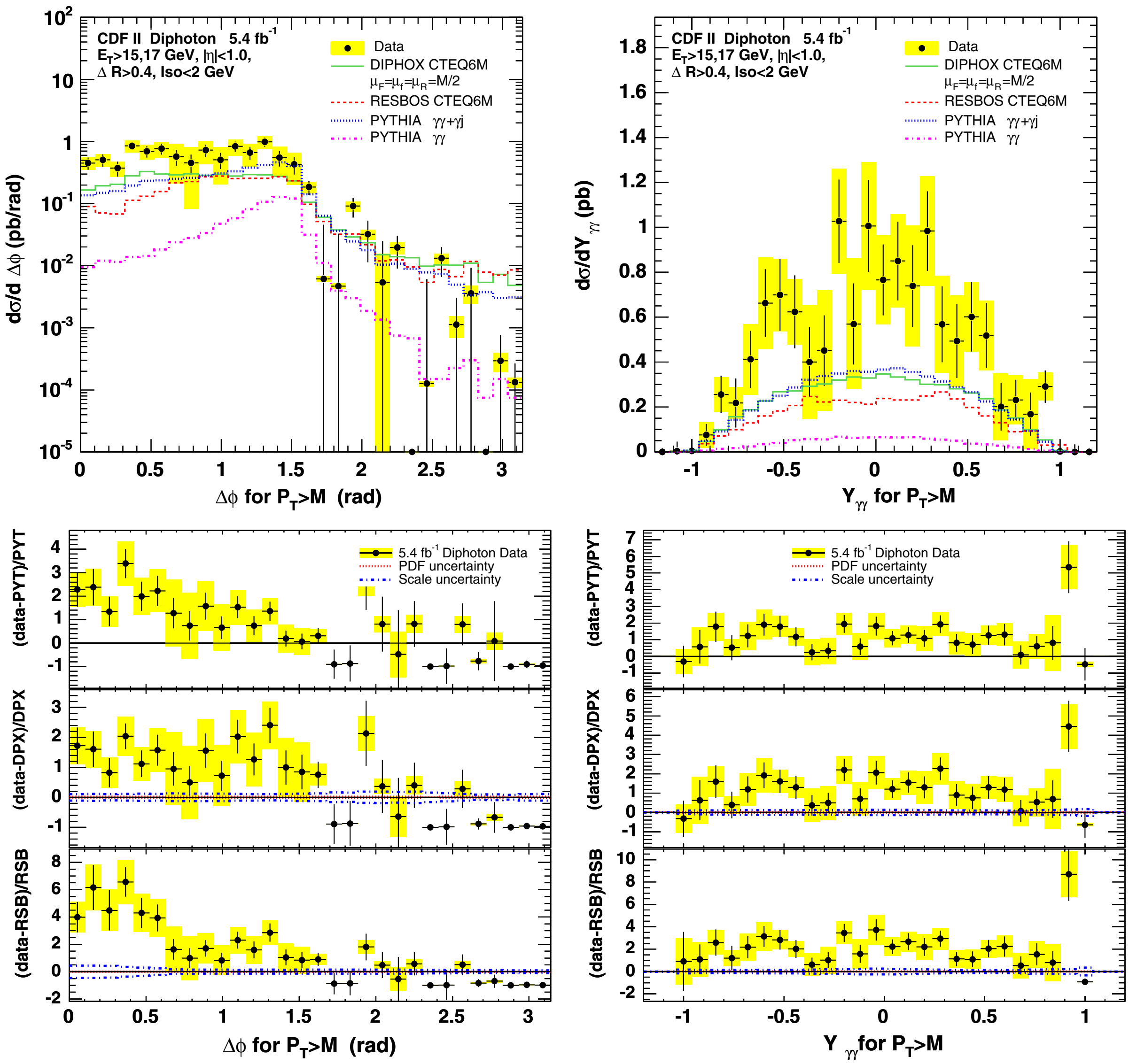

FIG. 20 (color online). The cross section as a function of the diphoton azimuthal distance (left) and of the diphoton rapidity (right) for $P_T > M$. *Top:* the absolute cross section values. *Bottom:* the relative deviations of the data from the predictions. *Note:* the vertical axes scales differ between relative deviation plots. The shaded area is the total systematic uncertainty in the data.

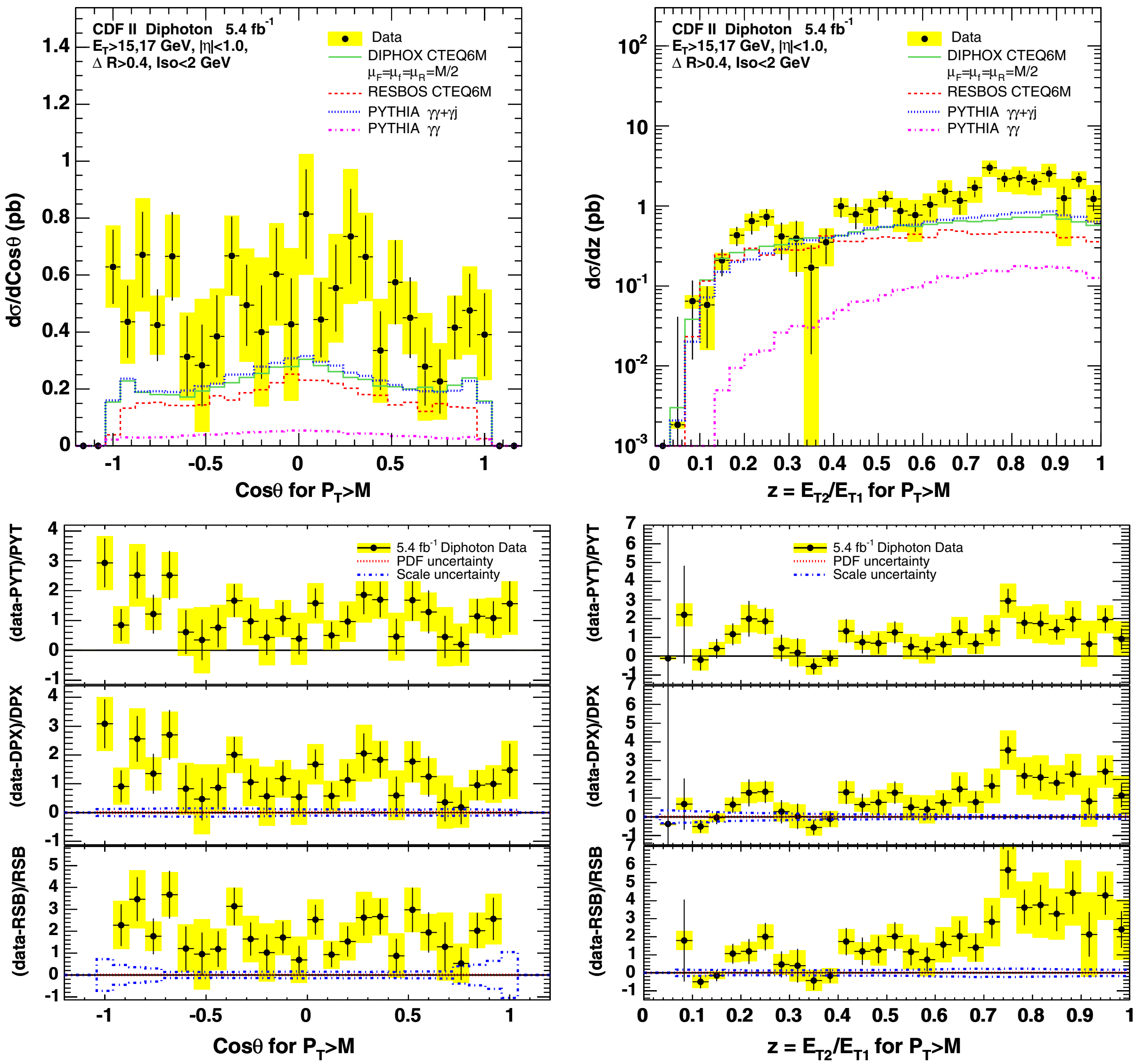

FIG. 21 (color online). The cross section as a function of the cosine of the polar angle in the Collins-Soper frame (left) and of the ratio of the subleading photon E_T to leading photon E_T (right) for $P_T > M$. *Top:* the absolute cross section values. *Bottom:* the relative deviations of the data from the predictions. *Note:* the vertical axes scales differ between relative deviation plots. The shaded area is the total systematic uncertainty in the data.

VI. CONCLUSIONS

In summary, the prompt diphoton production cross section, differential in kinematic variables sensitive to the dynamics of the reaction mechanism, is measured using data corresponding to an integrated luminosity of 5.36 fb^{-1} collected with the CDF II detector. The large size of the data sample allows for scanning a much more extended phase space and with a better statistical precision than in earlier measurements. Using a novel technique for the background subtraction, based on the track isolation, the overall systematic uncertainty is limited to about 30% on average.

The results of the measurement are compared with three state-of-the-art calculations, applying complementary techniques in modeling the reaction. All three calculations describe events with large diphoton mass and small diphoton transverse momentum fairly well, where the kinematics is similar to the decay of a low-P_T heavy particle, such as the Higgs boson, decaying into a photon pair. Exceptions are kinematic regions where gluon interactions and the associated fragmentations of quarks into photons are expected to be important, such as the low mass and azimuthal difference regions and the region of the Guillet shoulder at moderate transverse momentum. All three calculations underestimate the data in those regions. Although the DIPHOX calculation explicitly includes a fragmentation model, it fails to reproduce the data in those sensitive regions, possibly because of the approximate nature of the requirement of photon isolation in the

DIPHOX framework. This requirement is mostly responsible for the suppression of fragmentation contributions and is applied using hadron variables in the data but using parton variables in DIPHOX. The low transverse momentum and large azimuthal difference regions, where resummation in the diphoton transverse momentum is important, are best described by RESBOS, as expected from the analytical resummation implemented in this calculation. Photon radiation, especially from the initial-state quarks, in addition to the prompt photon production at the hard scattering, is for the first time shown to play a very important role in the parton showering PYTHIA calculation in order to bring the prediction into reasonable agreement with the data.

ACKNOWLEDGMENTS

We thank the Fermilab staff and the technical staffs of the participating institutions for their vital contributions. We also thank P. Nadolsky, C.-P. Yuan, Z. Li, J.-P. Guillet, C. Schmidt, and S. Mrenna for their valuable help in the theoretical calculations. This work was supported by the U.S. Department of Energy and National Science Foundation; the Italian Istituto Nazionale di Fisica Nucleare; the Ministry of Education, Culture, Sports, Science and Technology of Japan; the Natural Sciences and Engineering Research Council of Canada; the National Science Council of the Republic of China; the Swiss National Science Foundation; the A. P. Sloan Foundation; the Bundesministerium für Bildung und Forschung, Germany; the Korean World Class University Program, the National Research Foundation of Korea; the Science and Technology Facilities Council and the Royal Society, UK; the Institut National de Physique Nucleaire et Physique des Particules/CNRS; the Russian Foundation for Basic Research; the Ministerio de Ciencia e Innovación, and Programa Consolider-Ingenio 2010,

TABLE V. The diphoton production cross section differential in the diphoton invariant mass. The first error in the cross section is statistical and the second systematic.

Mass bin [GeV/c^2]	Cross section without cut [pb/(GeV/c^2)]	Cross section for $P_T < M$ [pb/(GeV/c^2)]	Cross section for $P_T > M$ [pb/(GeV/c^2)]
0–5	0	0	0
5–10	0.014 679 ± 0.002 997 ± 0.003 369	0	0.014 679 ± 0.002 997 ± 0.003 301
10–15	0.004 441 ± 0.000 607 ± 0.001 115	0	0.036 310 ± 0.004 965 ± 0.009 118
15–20	0.027 568 ± 0.005 232 ± 0.010 986	0	0.029 520 ± 0.005 602 ± 0.011 764
20–25	0.037 459 ± 0.005 482 ± 0.012 486	0.000 872 ± 0.000 686 ± 0.000 253	0.039 767 ± 0.005 921 ± 0.013 317
25–30	0.046 105 ± 0.006 060 ± 0.016 932	0.017 214 ± 0.004 129 ± 0.007 523	0.008 772 ± 0.001 367 ± 0.002 915
30–35	0.263 727 ± 0.014 488 ± 0.072 680	0.242 540 ± 0.013 891 ± 0.066 111	0.016 857 ± 0.003 275 ± 0.005 552
35–40	0.515 524 ± 0.020 876 ± 0.153 195	0.509 522 ± 0.021 070 ± 0.152 077	0.012 408 ± 0.002 360 ± 0.003 196
40–45	0.478 042 ± 0.018 964 ± 0.128 524	0.467 038 ± 0.018 734 ± 0.125 451	0.007 605 ± 0.002 024 ± 0.002 203
45–50	0.322 442 ± 0.015 234 ± 0.088 299	0.316 623 ± 0.015 079 ± 0.086 365	0.003 078 ± 0.001 149 ± 0.001 156
50–55	0.207 378 ± 0.011 824 ± 0.057 932	0.201 493 ± 0.011 730 ± 0.056 897	0.005 372 ± 0.001 299 ± 0.001 027
55–60	0.134 243 ± 0.009 249 ± 0.036 287	0.131 094 ± 0.009 184 ± 0.035 695	0.003 014 ± 0.001 053 ± 0.000 599
60–65	0.092 296 ± 0.007 243 ± 0.023 721	0.089 557 ± 0.007 169 ± 0.023 207	0.002 944 ± 0.001 071 ± 0.000 583
65–70	0.064 259 ± 0.006 117 ± 0.017 943	0.062 955 ± 0.006 080 ± 0.017 584	0.001 183 ± 0.000 629 ± 0.000 328
70–75	0.049 211 ± 0.005 194 ± 0.013 341	0.047 523 ± 0.005 150 ± 0.012 995	0.000 942 ± 0.000 396 ± 0.000 201
75–80	0.042 325 ± 0.004 477 ± 0.009 863	0.041 887 ± 0.004 449 ± 0.009 750	0.000 480 ± 0.000 536 ± 0.000 126
80–85	0.033 129 ± 0.003 469 ± 0.006 708	0.032 194 ± 0.003 436 ± 0.006 571	0.000 875 ± 0.000 443 ± 0.000 173
85–90	0.024 546 ± 0.003 230 ± 0.005 261	0.024 111 ± 0.003 194 ± 0.005 127	0.000 522 ± 0.000 577 ± 0.000 253
90–95	0.016 972 ± 0.002 675 ± 0.004 167	0.016 494 ± 0.002 657 ± 0.004 121	0.000 286 ± 0.000 191 ± 0.000 056
95–100	0.016 820 ± 0.002 418 ± 0.003 531	0.016 531 ± 0.002 401 ± 0.003 486	0.000 402 ± 0.000 405 ± 0.000 122
100–110	0.011 975 ± 0.001 421 ± 0.002 450	0.011 521 ± 0.001 407 ± 0.002 387	0.000 272 ± 0.000 118 ± 0.000 047
110–120	0.009 187 ± 0.001 193 ± 0.001 782	0.009 037 ± 0.001 182 ± 0.001 747	0.000 145 ± 0.000 156 ± 0.000 037
120–130	0.006 673 ± 0.000 968 ± 0.001 262	0.006 259 ± 0.000 953 ± 0.001 207	0.000 292 ± 0.000 119 ± 0.000 071
130–140	0.005 805 ± 0.000 856 ± 0.001 031	0.005 742 ± 0.000 848 ± 0.001 017	0.000 065 ± 0.000 109 ± 0.000 029
140–160	0.003 414 ± 0.000 448 ± 0.000 602	0.003 393 ± 0.000 444 ± 0.000 596	0.000 027 ± 0.000 072 ± 0.000 018
160–200	0.001 801 ± 0.000 208 ± 0.000 303	0.001 757 ± 0.000 206 ± 0.000 296	0.000 015 ± 0.000 009 ± 0.000 002
200–250	0.000 573 ± 0.000 107 ± 0.000 101	0.000 575 ± 0.000 107 ± 0.000 101	0
250–300	0.000 182 ± 0.000 055 ± 0.000 030	0.000 182 ± 0.000 055 ± 0.000 030	0
300–350	0.000 207 ± 0.000 055 ± 0.000 035	0.000 207 ± 0.000 055 ± 0.000 036	0
350–500	0.000 064 ± 0.000 017 ± 0.000 011	0.000 064 ± 0.000 017 ± 0.000 011	0

Spain; the Slovak R&D Agency; the Academy of Finland; and the Australian Research Council (ARC).

APPENDIX A: CONTENT LIKELIHOOD OF THE DATA SAMPLE

The signal and background disentanglement is done in a maximum likelihood framework. A likelihood of the composition of the baseline $\gamma\gamma$ sample is defined on the basis of binomial probabilities for the observed photons to pass or fail the track isolation cut

$$\mathcal{L} = \prod_{ik} \mu_i(k)^{n_i(k)} [1 - \mu_i(k)]^{1-n_i(k)} \tag{A1}$$

where $k = 1, \ldots, N$ labels all events in the sample and $i = pp, pf, fp, ff$ labels the categories of events in which both photons pass, the leading passes and the subleading fails, the leading fails and the subleading passes, and both photons fail the track isolation cut, respectively. $\mu_i(k)$ is the probability of the event k to fall in the category i and $n_i(k)$ is the observation for the event k; i.e., $n_i(k)$ is 1 for one of the four categories i and 0 for the other three. The probabilities can be analyzed as follows:

$$\mu_i(k) = \sum_j \varepsilon_{ij}(k) p_j(k) \tag{A2}$$

where $j = ss, sb, bs, bb$ labels the categories in which both photons are signal, the leading is signal and the subleading background, the leading is background and the subleading signal, and both photons are background, respectively. $p_j(k)$ is the probability for an event k to be in

TABLE VI. The diphoton production cross section differential in the diphoton transverse momentum. The first error in the cross section is statistical and the second systematic.

P_T bin [GeV/c]	Cross section without cut [pb/(GeV/c)]	Cross section for $P_T < M$ [pb/(GeV/c)]	Cross section for $P_T > M$ [pb/(GeV/c)]
0–1	0.276 549 ± 0.030 968 ± 0.067 613	0.276 542 ± 0.030 967 ± 0.067 612	0
1–2	0.823 081 ± 0.051 902 ± 0.184 444	0.823 132 ± 0.051 905 ± 0.184 456	0
2–3	1.043 320 ± 0.056 713 ± 0.236 673	1.043 373 ± 0.056 716 ± 0.236 685	0
3–4	1.026 369 ± 0.055 895 ± 0.241 145	1.026 574 ± 0.055 907 ± 0.241 193	0
4–5	0.913 944 ± 0.055 127 ± 0.234 272	0.914 185 ± 0.055 142 ± 0.234 334	0
5–6	0.908 628 ± 0.053 530 ± 0.215 222	0.909 148 ± 0.053 560 ± 0.215 345	0
6–7	0.784 121 ± 0.049 343 ± 0.200 779	0.784 624 ± 0.049 375 ± 0.200 908	0
7–8	0.606 111 ± 0.045 730 ± 0.166 151	0.606 435 ± 0.045 755 ± 0.166 240	0
8–9	0.538 172 ± 0.042 695 ± 0.159 898	0.538 651 ± 0.042 733 ± 0.160 040	0
9–10	0.416 951 ± 0.039 170 ± 0.125 580	0.417 071 ± 0.039 181 ± 0.125 616	0
10–12	0.371 872 ± 0.025 701 ± 0.113 307	0.372 199 ± 0.025 723 ± 0.113 406	0
12–14	0.275 282 ± 0.022 571 ± 0.089 464	0.275 797 ± 0.022 613 ± 0.089 631	0
14–16	0.196 349 ± 0.019 572 ± 0.072 611	0.196 591 ± 0.019 597 ± 0.072 700	0
16–18	0.179 301 ± 0.017 290 ± 0.060 538	0.179 549 ± 0.017 314 ± 0.060 622	0
18–20	0.125 584 ± 0.015 368 ± 0.045 351	0.126 581 ± 0.015 490 ± 0.045 711	0
20–25	0.127 625 ± 0.009 118 ± 0.038 128	0.125 027 ± 0.009 019 ± 0.037 597	0.001 932 ± 0.000 883 ± 0.000 457
25–30	0.092 613 ± 0.007 839 ± 0.028 973	0.078 351 ± 0.006 931 ± 0.024 441	0.013 751 ± 0.003 737 ± 0.004 417
30–35	0.087 187 ± 0.007 329 ± 0.027 382	0.040 507 ± 0.004 874 ± 0.012 880	0.049 065 ± 0.005 765 ± 0.015 309
35–40	0.056 515 ± 0.006 341 ± 0.020 793	0.024 564 ± 0.003 619 ± 0.007 531	0.033 546 ± 0.005 550 ± 0.014 138
40–45	0.039 824 ± 0.004 995 ± 0.012 246	0.012 094 ± 0.002 774 ± 0.004 861	0.030 706 ± 0.004 582 ± 0.008 315
45–50	0.022 650 ± 0.003 604 ± 0.006 110	0.010 569 ± 0.002 027 ± 0.002 311	0.012 983 ± 0.003 290 ± 0.004 252
50–60	0.018 204 ± 0.002 042 ± 0.004 416	0.006 578 ± 0.001 173 ± 0.001 669	0.012 472 ± 0.001 798 ± 0.002 971
60–70	0.007 542 ± 0.001 410 ± 0.002 019	0.003 080 ± 0.000 766 ± 0.000 693	0.004 862 ± 0.001 318 ± 0.001 481
70–80	0.005 717 ± 0.001 043 ± 0.001 271	0.001 773 ± 0.000 483 ± 0.000 331	0.004 388 ± 0.001 044 ± 0.001 080
80–90	0.003 467 ± 0.000 656 ± 0.000 676	0.000 801 ± 0.000 292 ± 0.000 167	0.003 387 ± 0.000 749 ± 0.000 642
90–100	0.001 355 ± 0.000 487 ± 0.000 377	0.000 079 ± 0.000 188 ± 0.000 103	0.001 242 ± 0.000 433 ± 0.000 279
100–120	0.001 057 ± 0.000 212 ± 0.000 281	0.000 198 ± 0.000 097 ± 0.000 062	0.000 972 ± 0.000 212 ± 0.000 239
120–140	0.000 655 ± 0.000 228 ± 0.000 135	0.000 059 ± 0.000 071 ± 0.000 017	0.000 516 ± 0.000 188 ± 0.000 094
140–160	0.000 287 ± 0.000 122 ± 0.000 051	0.000 008 ± 0.000 030 ± 0.000 007	0.001 222 ± 0.000 496 ± 0.000 227
160–200	0.000 100 ± 0.000 047 ± 0.000 021	0	0.000 227 ± 0.000 105 ± 0.000 039

the category j. $\varepsilon_{ij}(k)$ is the probability for an event k of the truth category j to be observed in the observation category i. This probability is directly related with the efficiencies of the two photons in the event k to pass the track isolation cut, since the efficiencies are defined as the probabilities for the leading or subleading photon to pass the cut. In a 4×4 matrix notation,

$$\varepsilon(k) = \begin{pmatrix} \epsilon_{s1}(k)\epsilon_{s2}(k) & \epsilon_{s1}(k)\epsilon_{b2}(k) & \epsilon_{b1}(k)\epsilon_{s2}(k) & \epsilon_{b1}(k)\epsilon_{b2}(k) \\ \epsilon_{s1}(k)(1-\epsilon_{s2}(k)) & \epsilon_{s1}(k)(1-\epsilon_{b2}(k)) & \epsilon_{b1}(k)(1-\epsilon_{s2}(k)) & \epsilon_{b1}(k)(1-\epsilon_{b2}(k)) \\ (1-\epsilon_{s1}(k))\epsilon_{s2}(k) & (1-\epsilon_{s1}(k))\epsilon_{b2}(k) & (1-\epsilon_{b1}(k))\epsilon_{s2}(k) & (1-\epsilon_{b1}(k))\epsilon_{b2}(k) \\ (1-\epsilon_{s1}(k))(1-\epsilon_{s2}(k)) & (1-\epsilon_{s1}(k))(1-\epsilon_{b2}(k)) & (1-\epsilon_{b1}(k))(1-\epsilon_{s2}(k)) & (1-\epsilon_{b1}(k))(1-\epsilon_{b2}(k)) \end{pmatrix} \quad \text{(A3)}$$

where $\epsilon_{\alpha\beta}(k)$ ($\alpha = s$ or b, $\beta = 1$ or 2) are the efficiencies of the leading or subleading photon, coming from the signal or from the background, to pass the track isolation cut.

TABLE VII. The diphoton production cross section differential in the diphoton azimuthal difference. The first error in the cross section is statistical and the second systematic.

$\Delta\phi$ bin [radians]	Cross section without cut [pb/rad]	Cross section for $P_T < M$ [pb/rad]	Cross section for $P_T > M$ [pb/rad]
0.000–0.105	0.456 343 ± 0.099 393 ± 0.099 826	0.008 959 ± 0.006 342 ± 0.004 135	0.455 591 ± 0.101 696 ± 0.101 433
0.105–0.209	0.443 854 ± 0.103 665 ± 0.101 738	0	0.506 682 ± 0.116 125 ± 0.114 737
0.209–0.314	0.346 811 ± 0.090 621 ± 0.085 583	0.000 964 ± 0.000 683 ± 0.000 446	0.377 053 ± 0.101 504 ± 0.096 562
0.314–0.419	0.805 494 ± 0.112 525 ± 0.174 161	0.008 695 ± 0.006 135 ± 0.001 692	0.835 398 ± 0.118 774 ± 0.181 144
0.419–0.524	0.621 352 ± 0.134 650 ± 0.162 677	0	0.668 658 ± 0.139 966 ± 0.168 432
0.524–0.628	0.695 012 ± 0.138 448 ± 0.183 259	0.007 809 ± 0.011 151 ± 0.001 958	0.712 287 ± 0.143 289 ± 0.188 042
0.628–0.733	0.553 260 ± 0.152 492 ± 0.264 377	0.023 257 ± 0.020 326 ± 0.006 509	0.528 230 ± 0.151 279 ± 0.258 421
0.733–0.838	0.375 583 ± 0.144 617 ± 0.261 528	0	0.433 524 ± 0.158 014 ± 0.270 138
0.838–0.942	0.671 584 ± 0.143 112 ± 0.228 641	0.029 115 ± 0.020 067 ± 0.010 039	0.679 242 ± 0.151 863 ± 0.231 038
0.942–1.047	0.522 112 ± 0.137 889 ± 0.219 688	0.038 178 ± 0.018 111 ± 0.008 311	0.496 178 ± 0.145 545 ± 0.230 738
1.047–1.152	0.864 793 ± 0.144 971 ± 0.220 201	0.087 654 ± 0.032 029 ± 0.018 939	0.781 381 ± 0.145 224 ± 0.207 021
1.152–1.257	0.798 674 ± 0.154 962 ± 0.224 791	0.150 640 ± 0.043 789 ± 0.033 689	0.638 090 ± 0.150 851 ± 0.210 793
1.257–1.361	1.124 851 ± 0.168 956 ± 0.257 447	0.188 806 ± 0.056 573 ± 0.044 931	0.939 944 ± 0.162 249 ± 0.212 925
1.361–1.466	0.639 906 ± 0.169 993 ± 0.284 205	0.118 937 ± 0.079 298 ± 0.074 899	0.527 203 ± 0.151 112 ± 0.210 203
1.466–1.571	0.834 419 ± 0.171 606 ± 0.270 175	0.421 297 ± 0.113 865 ± 0.107 330	0.408 768 ± 0.128 128 ± 0.171 398
1.571–1.676	1.250 665 ± 0.169 418 ± 0.311 391	1.007 357 ± 0.159 164 ± 0.278 003	0.230 173 ± 0.057 530 ± 0.047 005
1.676–1.780	0.832 275 ± 0.186 990 ± 0.364 452	0.826 622 ± 0.181 796 ± 0.334 001	0.006 883 ± 0.044 420 ± 0.000 755
1.780–1.885	1.001 287 ± 0.187 680 ± 0.340 539	0.998 464 ± 0.185 177 ± 0.326 921	0.004 982 ± 0.030 035 ± 0.000 548
1.885–1.990	1.076 470 ± 0.209 360 ± 0.442 750	0.985 068 ± 0.206 856 ± 0.435 764	0.097 539 ± 0.033 960 ± 0.017 947
1.990–2.094	1.667 315 ± 0.233 681 ± 0.501 973	1.628 501 ± 0.232 554 ± 0.498 599	0.030 895 ± 0.019 985 ± 0.005 693
2.094–2.199	2.275 603 ± 0.257 154 ± 0.585 295	2.271 233 ± 0.256 406 ± 0.580 308	0.005 091 ± 0.018 432 ± 0.007 031
2.199–2.304	1.982 347 ± 0.275 434 ± 0.703 905	1.945 552 ± 0.274 931 ± 0.703 233	0.021 202 ± 0.011 392 ± 0.004 164
2.304–2.409	3.180 244 ± 0.298 472 ± 0.883 152	3.185 517 ± 0.298 001 ± 0.878 647	0
2.409–2.513	3.344 205 ± 0.354 571 ± 1.099 021	3.345 126 ± 0.354 498 ± 1.097 423	0.000 142 ± 0.006 657 ± 0.000 016
2.513–2.618	4.913 562 ± 0.403 046 ± 1.447 020	4.883 607 ± 0.402 930 ± 1.445 024	0.010 602 ± 0.005 301 ± 0.001 996
2.618–2.723	6.787 434 ± 0.476 941 ± 1.881 799	6.788 491 ± 0.477 385 ± 1.881 996	0.000 988 ± 0.001 690 ± 0.000 302
2.723–2.827	9.949 192 ± 0.584 235 ± 2.773 900	9.948 025 ± 0.584 526 ± 2.773 673	0.001 445 ± 0.002 278 ± 0.000 396
2.827–2.932	14.781 949 ± 0.694 936 ± 3.966 263	14.791 632 ± 0.695 391 ± 3.968 861	0
2.932–3.037	21.597 660 ± 0.861 897 ± 5.826 928	21.602 392 ± 0.862 322 ± 5.828 225	0.000 218 ± 0.000 352 ± 0.000 061
3.037–3.142	33.827 076 ± 0.998 489 ± 8.203 793	33.825 920 ± 0.998 661 ± 8.204 532	0.000 133 ± 0.000 133 ± 0.000 024

The likelihood $\mathcal{L}$ is maximized or, equivalently, the opposite of its natural logarithm

$$L = -\ln\mathcal{L} = \sum_{ik}\{n_i(k)\ln\mu_i(k) + [1 - n_i(k)]\ln[1 - \mu_i(k)]\} \quad (A4)$$

is minimized with respect to the probabilities $p_j(k)$. The mini-
mization of the logarithm L leads to the system of equations

$$n_i(k) = \mu_i(k) = \sum_j \varepsilon_{ij}(k)p_j(k) \quad (A5)$$

with solutions

$$p_j(k) = \sum_i \varepsilon_{ji}^{-1}(k)n_i(k). \quad (A6)$$

The choice of the track isolation cut at 1 GeV/c gives the efficiencies $\epsilon_{\alpha\beta}(k)$ sufficient discriminating power among the truth categories j for the matrix $\varepsilon(k)$ to be nonsingular. By summing the probabilities over all events in the baseline sample, the maximum likelihood composition of the sample is obtained:

$$w_j = \sum_k p_j(k) = \sum_{ik} \varepsilon_{ji}^{-1}(k)n_i(k). \quad (A7)$$

Equation (A7) for the truth category $j = ss$ provides the signal fraction in the baseline $\gamma\gamma$ sample.

In general, the composition of a sample of events with m photons each can be resolved in a maximum likelihood framework by the inversion of a $2^m \times 2^m$ matrix, constructed as in Eq. (A3), which transforms the probability 2^m-vectors $p_j(k)$ to the observation 2^m-vectors $n_i(k)$. The generic matrix element $\varepsilon_{ij}(k)$ contains a factor $\epsilon_{\alpha\beta}(k)$ or

TABLE VIII. The diphoton production cross section differential in the diphoton rapidity. The first error in the cross section is statistical and the second systematic.

Y_{gg} bin	Cross section without cut [pb]	Cross section for $P_T < M$ [pb]	Cross section for $P_T > M$ [pb]
−1.20– − 1.12	0.047 796 ± 0.032 826 ± 0.014 355	0.047 253 ± 0.027 906 ± 0.017 471	0.000 543 ± 0.017 286 ± 0.000 059
−1.12– − 1.04	0.357 094 ± 0.120 949 ± 0.102 530	0.353 126 ± 0.113 517 ± 0.089 113	0.003 968 ± 0.041 744 ± 0.000 434
−1.04– − 0.96	0.187 965 ± 0.037 254 ± 0.047 292	0.179 976 ± 0.034 997 ± 0.041 721	0.004 941 ± 0.006 801 ± 0.004 111
−0.96– − 0.88	1.216 128 ± 0.179 918 ± 0.350 105	1.123 226 ± 0.169 654 ± 0.303 864	0.087 621 ± 0.056 102 ± 0.049 798
−0.88– − 0.80	2.934 750 ± 0.300 535 ± 0.734 394	2.634 538 ± 0.284 117 ± 0.653 983	0.284 037 ± 0.092 706 ± 0.076 637
−0.80– − 0.72	3.523 381 ± 0.364 743 ± 1.002 344	3.275 366 ± 0.344 374 ± 0.929 432	0.243 582 ± 0.121 183 ± 0.071 961
−0.72– − 0.64	4.727 782 ± 0.415 361 ± 1.224 628	4.251 420 ± 0.388 978 ± 1.079 371	0.442 221 ± 0.136 633 ± 0.142 010
−0.64– − 0.56	5.043 031 ± 0.463 117 ± 1.552 137	4.391 841 ± 0.437 811 ± 1.375 512	0.704 898 ± 0.160 548 ± 0.190 566
−0.56– − 0.48	6.849 294 ± 0.521 381 ± 1.783 643	6.156 165 ± 0.496 178 ± 1.631 273	0.704 821 ± 0.161 752 ± 0.160 419
−0.48– − 0.40	7.515 287 ± 0.565 874 ± 1.957 807	6.894 050 ± 0.542 207 ± 1.818 195	0.612 712 ± 0.159 704 ± 0.141 450
−0.40– − 0.32	7.432 176 ± 0.605 607 ± 2.230 531	7.009 432 ± 0.582 405 ± 2.029 948	0.387 476 ± 0.149 935 ± 0.191 711
−0.32– − 0.24	9.473 290 ± 0.644 927 ± 2.438 148	9.018 377 ± 0.624 024 ± 2.249 574	0.448 143 ± 0.156 451 ± 0.207 981
−0.24– − 0.16	9.171 682 ± 0.650 452 ± 2.482 947	8.178 396 ± 0.625 007 ± 2.276 978	1.030 157 ± 0.186 527 ± 0.232 884
−0.16– − 0.08	10.391 827 ± 0.673 024 ± 2.604 154	9.833 859 ± 0.649 550 ± 2.409 783	0.581 114 ± 0.183 635 ± 0.235 125
−0.08–0	10.685 762 ± 0.683 909 ± 2.779 428	9.737 009 ± 0.655 963 ± 2.536 669	1.011 320 ± 0.205 173 ± 0.258 684
0–0.08	9.778 326 ± 0.680 032 ± 2.746 355	8.910 962 ± 0.656 693 ± 2.541 139	0.779 653 ± 0.160 122 ± 0.189 297
0.08–0.16	10.245 283 ± 0.664 715 ± 2.572 113	9.428 201 ± 0.642 795 ± 2.382 707	0.844 021 ± 0.173 754 ± 0.196 508
0.16–0.24	8.898 950 ± 0.650 517 ± 2.522 506	8.174 833 ± 0.625 682 ± 2.299 986	0.740 208 ± 0.181 740 ± 0.229 029
0.24–0.32	9.873 399 ± 0.639 878 ± 2.378 116	8.881 087 ± 0.614 339 ± 2.143 591	0.980 913 ± 0.177 119 ± 0.232 361
0.32–0.40	8.208 516 ± 0.599 002 ± 2.150 160	7.608 601 ± 0.571 739 ± 1.962 087	0.575 259 ± 0.170 775 ± 0.186 692
0.40–0.48	8.310 832 ± 0.582 531 ± 2.114 900	7.805 289 ± 0.557 393 ± 1.950 114	0.489 608 ± 0.162 967 ± 0.168 822
0.48–0.56	6.158 322 ± 0.525 197 ± 1.682 342	5.551 052 ± 0.501 466 ± 1.536 281	0.602 316 ± 0.155 006 ± 0.146 833
0.56–0.64	5.764 018 ± 0.484 449 ± 1.615 546	5.254 852 ± 0.463 164 ± 1.480 387	0.515 143 ± 0.143 704 ± 0.136 823
0.64–0.72	3.746 496 ± 0.413 343 ± 1.272 077	3.516 958 ± 0.394 670 ± 1.144 314	0.219 857 ± 0.116 288 ± 0.126 414
0.72–0.80	2.638 815 ± 0.344 297 ± 0.937 298	2.365 470 ± 0.327 398 ± 0.833 140	0.236 348 ± 0.092 090 ± 0.090 185
0.80–0.88	1.908 901 ± 0.278 836 ± 0.661 709	1.745 827 ± 0.263 054 ± 0.558 774	0.178 584 ± 0.101 977 ± 0.123 069
0.88–0.96	1.342 328 ± 0.185 391 ± 0.348 576	1.092 484 ± 0.174 767 ± 0.311 890	0.266 332 ± 0.065 150 ± 0.055 395
0.96–1.04	0.125 836 ± 0.034 791 ± 0.043 927	0.121 207 ± 0.033 430 ± 0.042 727	0.002 452 ± 0.004 579 ± 0.000 700
1.04–1.12	0.251 782 ± 0.113 387 ± 0.068 974	0.278 853 ± 0.108 155 ± 0.064 602	0
1.12–1.20	0.001 304 ± 0.029 359 ± 0.000 143	0.001 304 ± 0.029 359 ± 0.000 143	0

TABLE IX. The diphoton production cross section differential in the cosine of the polar angle in the Collins-Soper frame. The first error in the cross section is statistical and the second systematic.

$\cos\theta$ bin	Cross section without cut [pb]	Cross section for $P_T < M$ [pb]	Cross section for $P_T > M$ [pb]
−1.20– − 1.12	0	0	0
−1.12– − 1.04	0	0	0
−1.04– − 0.96	0.696 711 ± 0.146 723 ± 0.155 742	0.000 604 ± 0.012 602 ± 0.000 066	0.679 356 ± 0.141 129 ± 0.153 197
−0.96– − 0.88	0.593 058 ± 0.160 701 ± 0.183 348	0.043 900 ± 0.032 514 ± 0.018 749	0.534 910 ± 0.155 592 ± 0.157 684
−0.88– − 0.80	0.901 409 ± 0.165 027 ± 0.221 503	0.214 033 ± 0.066 821 ± 0.046 916	0.679 008 ± 0.152 504 ± 0.179 300
−0.80– − 0.72	0.964 840 ± 0.155 297 ± 0.234 473	0.686 284 ± 0.131 504 ± 0.167 953	0.394 443 ± 0.116 872 ± 0.094 604
−0.72– − 0.64	2.322 500 ± 0.330 788 ± 0.674 056	1.895 647 ± 0.321 399 ± 0.603 007	0.702 685 ± 0.163 956 ± 0.152 732
−0.64– − 0.56	3.911 811 ± 0.353 577 ± 0.984 306	3.971 193 ± 0.364 919 ± 0.976 839	0.308 842 ± 0.140 763 ± 0.123 241
−0.56– − 0.48	4.225 161 ± 0.385 762 ± 1.118 926	4.381 881 ± 0.405 094 ± 1.105 399	0.225 221 ± 0.114 141 ± 0.141 418
−0.48– − 0.40	5.878 916 ± 0.500 103 ± 1.841 742	5.998 004 ± 0.523 626 ± 1.862 583	0.328 751 ± 0.123 479 ± 0.118 609
−0.40– − 0.32	8.447 426 ± 0.558 218 ± 2.115 941	8.476 556 ± 0.589 264 ± 2.168 045	0.611 133 ± 0.126 341 ± 0.129 931
−0.32– − 0.24	8.006 947 ± 0.563 629 ± 2.281 457	8.205 863 ± 0.595 600 ± 2.316 283	0.424 552 ± 0.122 576 ± 0.141 255
−0.24– − 0.16	9.621 518 ± 0.610 748 ± 2.601 253	10.100 368 ± 0.646 808 ± 2.669 680	0.352 094 ± 0.144 908 ± 0.177 738
−0.16– − 0.08	11.031 545 ± 0.647 516 ± 3.074 353	11.400 319 ± 0.685 597 ± 3.182 760	0.544 025 ± 0.146 581 ± 0.146 555
−0.08–0	11.701 358 ± 0.652 059 ± 3.229 385	12.252 276 ± 0.687 876 ± 3.313 652	0.409 344 ± 0.154 987 ± 0.199 857
0–0.08	10.744 885 ± 0.639 661 ± 3.180 184	10.786 094 ± 0.672 314 ± 3.242 347	0.808 290 ± 0.156 327 ± 0.195 042
0.08–0.16	10.215 599 ± 0.620 273 ± 2.867 342	10.599 528 ± 0.657 294 ± 2.971 375	0.475 211 ± 0.141 936 ± 0.137 377
0.16–0.24	8.894 859 ± 0.591 847 ± 2.681 245	9.066 109 ± 0.621 564 ± 2.735 215	0.593 223 ± 0.163 517 ± 0.176 269
0.24–0.32	8.996 937 ± 0.573 034 ± 2.308 823	9.083 449 ± 0.602 347 ± 2.317 747	0.814 932 ± 0.184 770 ± 0.227 355
0.32–0.40	8.131 862 ± 0.550 158 ± 2.082 427	8.160 151 ± 0.578 638 ± 2.111 536	0.687 574 ± 0.151 101 ± 0.156 505
0.40–0.48	7.136 364 ± 0.535 862 ± 1.790 615	7.337 457 ± 0.558 791 ± 1.797 939	0.363 666 ± 0.150 402 ± 0.157 323
0.48–0.56	6.314 780 ± 0.443 943 ± 1.479 071	6.414 981 ± 0.468 845 ± 1.498 226	0.642 568 ± 0.164 994 ± 0.156 587
0.56–0.64	4.206 630 ± 0.370 591 ± 1.022 774	4.311 754 ± 0.395 680 ± 1.044 270	0.438 339 ± 0.137 911 ± 0.112 795
0.64–0.72	2.507 368 ± 0.287 244 ± 0.605 107	2.372 216 ± 0.277 399 ± 0.544 206	0.242 620 ± 0.118 928 ± 0.127 240
0.72–0.80	0.723 595 ± 0.163 114 ± 0.254 653	0.508 954 ± 0.128 116 ± 0.162 397	0.253 995 ± 0.126 498 ± 0.118 790
0.80–0.88	0.553 629 ± 0.131 739 ± 0.141 735	0.117 661 ± 0.060 000 ± 0.032 288	0.422 761 ± 0.113 453 ± 0.106 068
0.88–0.96	0.486 210 ± 0.125 296 ± 0.141 378	0.046 081 ± 0.036 977 ± 0.015 266	0.420 675 ± 0.114 459 ± 0.120 587
0.96–1.04	0.389 773 ± 0.141 480 ± 0.142 265	0.014 859 ± 0.023 566 ± 0.010 889	0.372 354 ± 0.138 736 ± 0.128 626
1.04–1.12	0	0	0
1.12–1.20	0	0	0

$1 - \epsilon_{\alpha\beta}(k)$ for each photon $\beta = 1, 2, \ldots, m$ with $\alpha = s$ (b) if the photon is signal (background) in the truth category j and passes or fails, respectively, the track isolation cut in the observation category i. In this context, Eq. (1) for the single-photon sample is derived from Eq. (A7) by inverting for each event the matrix

$$\varepsilon = \begin{pmatrix} \epsilon_s & \epsilon_b \\ 1-\epsilon_s & 1-\epsilon_b \end{pmatrix} \Rightarrow \varepsilon^{-1} = \frac{1}{\epsilon_s - \epsilon_b}\begin{pmatrix} 1-\epsilon_b & -\epsilon_b \\ -1+\epsilon_s & \epsilon_s \end{pmatrix} \tag{A8}$$

with observation vectors

$$n_p = \begin{pmatrix} 1 \\ 0 \end{pmatrix} \qquad n_f = \begin{pmatrix} 0 \\ 1 \end{pmatrix} \tag{A9}$$

for photons passing (n_p) or failing (n_f) the track isolation cut. Equation (A7) then gives for the signal fraction of the single-photon sample

$$w_s = \sum_p \left(\frac{1-\epsilon_b}{\epsilon_s - \epsilon_b}\right)_p + \sum_f \left(\frac{-\epsilon_b}{\epsilon_s - \epsilon_b}\right)_f = \sum_i \left(\frac{\epsilon - \epsilon_b}{\epsilon_s - \epsilon_b}\right)_i \tag{A10}$$

where, in the first line, the first sum runs over all photons passing the cut and the second sum runs over all photons failing the cut. Equation (A10) is identical with Eq. (1).

APPENDIX B: CROSS SECTION TABLES

This appendix provides Tables V, VI, VII, VIII, IX, and X, which list the measured differential cross section values as functions of the six kinematic variables selected in this analysis. Each table lists the bins of the selected variable, the values of the cross section in the respective bins for the three examined cases of no kinematic cut, $P_T < M$, and $P_T > M$, and the statistical and total systematic uncertainties associated with each cross section value.

TABLE X. The diphoton production cross section differential in the subleading to leading photon transverse momentum ratio. The first error in the cross section is statistical and the second systematic.

z bin	Cross section without cut [pb]	Cross section for $P_T < M$ [pb]	Cross section for $P_T > M$ [pb]
0–0.033	0	0	0
0.033–0.067	0.001 845 ± 0.039 308 ± 0.000 183	0	0.001 845 ± 0.039 308 ± 0.000 183
0.067–0.100	0.064 683 ± 0.052 631 ± 0.011 964	0	0.064 683 ± 0.052 631 ± 0.011 541
0.100–0.133	0.040 160 ± 0.027 228 ± 0.018 852	0.014 680 ± 0.032 433 ± 0.004 628	0.059 705 ± 0.042 528 ± 0.042 287
0.133–0.167	0.208 681 ± 0.066 194 ± 0.042 837	0.011 290 ± 0.006 518 ± 0.002 107	0.219 178 ± 0.080 746 ± 0.052 940
0.167–0.200	0.581 526 ± 0.144 204 ± 0.158 584	0.130 976 ± 0.080 148 ± 0.047 058	0.421 745 ± 0.112 886 ± 0.095 122
0.200–0.233	0.687 775 ± 0.179 968 ± 0.138 709	0.220 290 ± 0.099 866 ± 0.041 656	0.624 676 ± 0.198 432 ± 0.138 087
0.233–0.267	0.882 504 ± 0.219 745 ± 0.200 850	0.311 307 ± 0.158 139 ± 0.120 736	0.662 516 ± 0.169 350 ± 0.152 908
0.267–0.300	1.254 394 ± 0.290 529 ± 0.272 821	0.891 524 ± 0.232 063 ± 0.173 525	0.380 905 ± 0.188 202 ± 0.125 645
0.300–0.333	0.742 542 ± 0.342 084 ± 0.399 154	0.427 234 ± 0.266 842 ± 0.247 371	0.362 702 ± 0.241 421 ± 0.173 907
0.333–0.367	0.633 573 ± 0.347 426 ± 0.629 057	0.465 991 ± 0.313 708 ± 0.505 393	0.171 920 ± 0.157 777 ± 0.130 833
0.367–0.400	2.120 037 ± 0.452 224 ± 0.852 624	1.715 373 ± 0.410 393 ± 0.695 311	0.360 338 ± 0.169 736 ± 0.140 800
0.400–0.433	3.736 916 ± 0.590 222 ± 1.123 369	2.770 300 ± 0.524 436 ± 0.913 390	1.008 748 ± 0.280 388 ± 0.241 464
0.433–0.467	3.631 943 ± 0.628 078 ± 1.112 420	2.889 061 ± 0.570 550 ± 0.962 623	0.784 327 ± 0.273 687 ± 0.172 160
0.467–0.500	4.521 544 ± 0.752 621 ± 1.788 419	3.644 498 ± 0.692 765 ± 1.516 931	0.862 816 ± 0.286 054 ± 0.268 761
0.500–0.533	4.504 285 ± 0.765 007 ± 2.208 000	3.370 450 ± 0.701 471 ± 2.016 244	1.208 186 ± 0.316 267 ± 0.270 012
0.533–0.567	5.323 637 ± 0.834 206 ± 2.560 178	4.458 064 ± 0.775 756 ± 2.247 832	0.852 710 ± 0.299 524 ± 0.308 661
0.567–0.600	7.041 574 ± 0.923 763 ± 2.652 894	6.228 433 ± 0.870 212 ± 2.309 346	0.758 477 ± 0.289 013 ± 0.321 800
0.600–0.633	8.403 337 ± 1.002 178 ± 3.176 046	7.326 917 ± 0.951 026 ± 2.835 386	1.050 768 ± 0.308 693 ± 0.336 094
0.633–0.667	10.720 245 ± 1.130 024 ± 3.698 758	9.382 812 ± 1.061 512 ± 3.277 018	1.561 377 ± 0.447 592 ± 0.490 694
0.667–0.700	12.252 908 ± 1.215 009 ± 4.376 297	11.087 163 ± 1.154 250 ± 4.032 151	1.190 425 ± 0.387 427 ± 0.352 079
0.700–0.733	16.415 794 ± 1.325 045 ± 5.439 192	14.773 602 ± 1.265 468 ± 4.943 280	1.709 796 ± 0.404 441 ± 0.516 840
0.733–0.767	24.203 773 ± 1.475 829 ± 6.110 600	21.437 672 ± 1.403 616 ± 5.494 815	2.989 357 ± 0.484 161 ± 0.680 585
0.767–0.800	25.442 360 ± 1.568 095 ± 6.926 982	23.305 996 ± 1.500 378 ± 6.332 095	2.170 811 ± 0.461 754 ± 0.605 827
0.800–0.833	26.262 505 ± 1.639 982 ± 7.542 237	24.221 176 ± 1.570 060 ± 6.897 027	2.164 903 ± 0.503 890 ± 0.696 416
0.833–0.867	33.239 754 ± 1.758 692 ± 8.786 769	31.182 541 ± 1.696 572 ± 8.184 977	2.019 600 ± 0.455 356 ± 0.595 763
0.867–0.900	43.423 592 ± 1.926 264 ± 10.230 121	41.122 257 ± 1.860 713 ± 9.587 927	2.478 693 ± 0.538 976 ± 0.732 571
0.900–0.933	41.876 434 ± 1.940 630 ± 9.835 004	40.736 725 ± 1.885 258 ± 9.372 191	1.262 268 ± 0.497 901 ± 0.732 053
0.933–0.967	46.414 635 ± 2.069 529 ± 10.663 040	44.152 313 ± 2.017 412 ± 10.112 022	2.116 757 ± 0.431 365 ± 0.515 146
0.967–1.000	43.381 981 ± 2.094 066 ± 10.489 670	41.883 457 ± 2.042 450 ± 9.953 175	1.217 864 ± 0.363 204 ± 0.483 372

[1] T. Aaltonen *et al.* (CDF Collaboration), Phys. Rev. Lett. **103**, 061803 (2009); V. M. Abazov *et al.* (D0 Collaboration), Phys. Rev. Lett. **102**, 231801 (2009); G. Aad *et al.* (ATLAS Collaboration), arXiv:0901.0512; G. L. Bayatian *et al.* (CMS Collaboration), J. Phys. G **34**, 995 (2007).

[2] T. Aaltonen *et al.* (CDF Collaboration), Phys. Rev. Lett. **99**, 171801 (2007); Phys. Rev. D **83**, 011102 (2011); K. W. Bell *et al.* (CMS Collaboration), J. High Energy Phys. 05 (2011) 085; ATLAS Collaboration, arXiv:1107.0561v2.

[3] T. Sjöstrand, Comput. Phys. Commun. **82**, 74 (1994); S. Mrenna, Comput. Phys. Commun. **101**, 232 (1997).

[4] G. Corcella, I. G. Knowles, G. Marchesini, S. Moretti, K. Odagiri, P. Richardson, M. H. Seymour, and B. R. Webber, J. High Energy Phys. 01 (2001) 010.

[5] S. Höche, S. Schumann, and F. Siegert, Phys. Rev. D **81**, 034026 (2010).

[6] T. Binoth, J. P. Guillet, E. Pilon, and M. Werlen, Eur. Phys. J. C **16**, 311 (2000); Phys. Rev. D **63**, 114016 (2001).

[7] Z. Bern, L. Dixon, and C. Schmidt, Phys. Rev. D **66**, 074018 (2002).

[8] C. Balazs, E. L. Berger, P. Nadolsky, and C.-P. Yuan, Phys. Rev. D **637**, 235 (2006); **76**, 013009 (2007); **76**, 013008 (2007).

[9] L. Bourhis, M. Fontannaz, and J. P. Guillet, Eur. Phys. J. C **2**, 529 (1998).

[10] D. Acosta *et al.* (CDF Collaboration), Phys. Rev. Lett. **95**, 022003 (2005).

[11] V. M. Abazov *et al.* (D0 Collaboration), Phys. Lett. B **690**, 108 (2010).

[12] The CDF II detector uses a cylindrical coordinate system in which ϕ is the azimuthal angle, θ is the polar angle with respect to the proton beam, r is the radius from the nominal beam line, and z points in the proton beam direction, with the origin at the center of the detector. The transverse $r - \phi$, or $x - y$ plane, is the plane perpendicular to the z axis. The pseudorapidity, η, is defined as $-\ln(\tan(\theta/2))$. For the photons, which have zero mass, this is identical to the rapidity $y = \tanh^{-1}(p_z/E)$, where $p_z = p \cdot \cos\theta$ is the momentum parallel to the beam [13].

The transverse energy of a particle is $E_T = E \cdot \sin\theta$. The transverse momentum of a particle is defined as $p_T = p \cdot \sin\theta$.
[13] W. M. Yao *et al.*, J. Phys. G **33**, 31 (2006).
[14] D. Acosta *et al.* (CDF Collaboration), Phys. Rev. D **71**, 032001 (2005).
[15] C. S. Hill *et al.*, Nucl. Instrum. Methods Phys. Res., Sect. A **511**, 118 (2003).
[16] A. Sill *et al.*, Nucl. Instrum. Methods Phys. Res., Sect. A **447**, 1 (2000).
[17] A. Affolder *et al.* (CDF Collaboration), Nucl. Instrum. Methods Phys. Res., Sect. A **453**, 84 (2000).
[18] A. Affolder *et al.* (CDF Collaboration), Nucl. Instrum. Methods Phys. Res., Sect. A **526**, 249 (2004).
[19] L. Balka *et al.*, Nucl. Instrum. Methods Phys. Res., Sect. A **267**, 272 (1988); S. R. Hahn *et al.*, *ibid.* **267**, 351 (1988).
[20] S. Bertolucci *et al.*, Nucl. Instrum. Methods Phys. Res., Sect. A **267**, 301 (1988).
[21] M. Goncharov *et al.*, Nucl. Instrum. Methods Phys. Res., Sect. A **565**, 543 (2006).
[22] D. Acosta *et al.*, Nucl. Instrum. Methods Phys. Res., Sect. A **494**, 57 (2002).
[23] F. Abe *et al.* (CDF Collaboration), Nucl. Instrum. Methods Phys. Res., Sect. A **271**, 387 (1988).
[24] For the central calorimeter, the fiducial region covers ~87% of the total area.
[25] T. Aaltonen *et al.* (CDF Collaboration), Phys. Rev. D **82**, 052005 (2010).
[26] E. Gerchtein and M. Paulini, in *2003 Computing in High Energy and Nuclear Physics (CHEP03), La Jolla, CA, 2003*, econf C0303241, TUMT005 (2003); the version of GEANT used for the detector simulation is 3.21. See the CERN Program Library Long Writeup W5013.
[27] T. Aaltonen *et al.* (CDF Collaboration), Phys. Rev. D **77**, 092001 (2008); Phys. Rev. Lett. **102**, 232002 (2009).
[28] H. L. Lai, J. Huston, S. Kuhlmann, J. Morfin, F. Olness, J. F. Owens, J. Pumplin, and W. K. Tung, Eur. Phys. J. C **12**, 375 (2000).
[29] R. Field and C. Group, arXiv:0510198.
[30] T. Aaltonen *et al.* (CDF Collaboration), Phys. Rev. D **80**, 111106 (2009).
[31] D. Acosta *et al.* (CDF Collaboration), Phys. Rev. Lett. **94**, 091803 (2005).
[32] J. Pumplin, D. R. Stump, J. Huston, H. L. Lai, P. Nadolsky, and W. K. Tung, J. High Energy Phys. 07 (2002) 012.
[33] J. C. Collins and D. E. Soper, Phys. Rev. D **16**, 2219 (1977).